# TORC2-Gad8 dependent myosin phosphorylation modulates regulation by calcium.

Karen Baker[1], Irene A. Gyamfi[1], Gregory I. Mashanov[2], Justin E. Molloy[2], Michael A. Geeves[1] and Daniel P. Mulvihill[1,3]

[1] School of Biosciences, University of Kent, Canterbury, Kent, CT2 7NJ, UK.

[2] The Francis Crick Institute, 1 Midland Road, London NW1 1AT, UK

[3] Author for correspondence e-mail: d.p.mulvihill@kent.ac.uk
Tel: +44 (0) 1227 827239

Key words: pombe, endocytosis, calmodulin, Tor kinase.

Running Title: Phosphorylation & calcium co-dependent myosin regulation

**Abstract**

Cells respond to changes in their environment through signalling networks that modulate cytoskeleton and membrane organisation to coordinate cell cycle progression, polarised cell growth and multicellular development. Here, we define a novel regulatory mechanism by which the motor activity and function of the fission yeast type 1 myosin, Myo1, is modulated by TORC2 signalling dependent phosphorylation. Phosphorylation of the conserved serine at position 742 within the neck region changes both the conformation of the neck region and the interactions between Myo1 and its associating calmodulin light chains. S742 phosphorylation thereby couples calcium and TOR signalling networks in the modulation of myosin-1 dynamics to co-ordinate actin polymerisation and membrane reorganisation at sites of endocytosis and polarised cell growth in response to environmental and cell cycle cues.

## Introduction

The actin cytoskeleton underpins cellular organisation by maintaining cell shape through the transmission of mechanical signals between the cell periphery and nucleus, to influence protein expression, organisation and cellular architecture in response to needs of the cell. Myosins, actin-associated motor-proteins, work in collaboration with an array of actin-binding proteins to facilitate global cytoskeletal reorganisation and a plethora of other processes including cell migration, intracellular transport, tension sensing and cell division (O'Connell *et al*, 2007). Each of the many classes of myosin contain three distinct domains: an actin-binding ATPase motor domain, that exerts force against actin, a lever arm or neck region that contains light chain binding IQ motifs, and a tail region which specifies cargo binding and other molecular interactions.

Although the different classes of myosin perform very different cellular functions, they all operate via the same basic mechanism: the motor domain undergoes cyclical interactions with actin coupled to the breakdown of ATP. Each molecule of ATP that is converted to ADP and inorganic phosphate can generate movement along actin of between 5-25 nm and force of up to 5 pN. Regulation of acto-myosin motility is multi-faceted (Heissler & Sellers, 2016a), combining regulatory pathways operating via the actin track (historically called thin-filament regulation), or myosin-linked regulation (historically called thick-filament regulation). This latter control is often mediated via phosphorylation of the heavy chain or light chain(s), or by calcium-regulation of light chain binding (Heissler & Sellers, 2016b). Phosphorylation at the conserved “TEDS” site motif within the myosin motor domain of class 1 myosin affects acto-myosin interaction (Bement & Mooseker, 1995), while phosphorylation within the tail region of class 5 myosin controls cargo binding (Rogers *et al*, 1999). In contrast, phosphorylation of class 2 myosin light chains and/or heavy chain can change the folded state of the heavy chain to alter actin interaction and the ability to form filaments (Redowicz, 2001; Kendrick-Jones *et al*, 1987; Pasapera *et al*, 2015). Thus, phosphoregulation of myosin can occur in the head, neck and tail regions, as well as the light chains, and its impact vary across myosin classes and between paralogues within the same class. The

impact of phosphorylation upon the motile function of most myosins remains to be established.

The genome of the fission yeast, *Schizosaccharomyces pombe*, encodes five myosin heavy chains from classes 1, 2, and 5 (Win *et al*, 2002). The single class 1 myosin (UniProt Accession: Q9Y7Z8), here termed Myo1, is a 135 kDa protein, with motor domain, neck region (with two canonical IQ motifs) and a 49 kDa tail region containing a, so-called, myosin tail-homology-2 domain (MYTH-2), a membrane-binding pleckstrin homology (PH) domain, an SH3 domain and a carboxyl-terminal acidic region. The acidic region associates with, and activates, the Arp2/3 complex to nucleate actin polymerisation (Lee *et al*, 2000). The myosin motor has a conserved TEDS site, which is phosphorylated to modulate the protein's ability to associate with actin (Attanapola *et al*, 2009). Myo1 associates with membranes, primarily at sites of cell growth, where it is required for endocytosis, actin organisation and spore formation (Sirotkin *et al*, 2005; Lee *et al*, 2000; Itadani *et al*, 2007).

Calmodulin or calmodulin-like light chains associate with the IQ motifs within the myosin neck to regulate both the length and stiffness of the lever arm (Trybus *et al*, 2007) and behaviour of the motor domain (Adamek *et al*, 2008). Calmodulins are ubiquitous calcium binding proteins that associate with and regulate the cellular function of diverse proteins. Calcium associates with up to four EF hand motifs within the calmodulin molecule to instigate a conformational change that modulates its affinity for IQ motifs (Crivici & Ikura, 1995).

*S. pombe* encodes for two calmodulin like proteins, Cam1 and Cam2 (Takeda & Yamamoto, 1987; Itadani *et al*, 2007). Cam1 is a typical calmodulin that associates with IQ domain containing proteins in a calcium dependent manner, to modulate functions as diverse as endocytosis, spore formation, cell division and spindle pole body integrity (Takeda & Yamamoto, 1987; Moser *et al*, 1995; 1997; Itadani *et al*, 2010). Although Cam2 shares Cam1's ability to regulate Myo1, Cam2 differs from Cam1 in two important respects:

Cam2 is not essential for viability and is predicted to be insensitive to calcium (Sammons *et al*, 2011; Itadani *et al*, 2007). Furthermore, while cells lacking Cam2 show defects in spore formation following sexual differentiation they have no significant growth-associated phenotypes during the vegetative growth cycle.

TOR (Target of Rapamycin) signaling plays a key role in modulating cell growth in response to changes in cell cycle status and environmental conditions from yeast to man (Laplante & Sabatini, 2012; Hartmuth & Petersen, 2009). The mTOR kinase forms two distinct protein complexes TOR complex 1 (TORC1) and TOR complex 2 (TORC2), that are each defined by unique components, that are highly conserved across species. TORC1 contains the Regulatory Associated Protein of mTOR (RAPTOR), whereas in TORC2 RAPTOR is replaced with the Rapamycin-Insensitive Companion Of mTOR (RICTOR). Both TORC1 and TORC2 complexes control cell migration and F-actin organisation (Liu & Parent, 2011). TORC2 plays a key role in regulating the actin cytoskeleton in yeasts, *Dictyostelium discoideum* and mammalian cells, modulating actin organisation and growth in response to cell cycle progression and the cellular environment (Jacinto *et al*, 2004; Baker *et al*, 2016; Lee *et al*, 2005).

In *S. pombe*, TORC2 recruits and phosphorylates the fission yeast AGC kinase, Gad8 (Matsuo, 2003), a homologue of human SGK1/2 kinase to regulate cell proliferation, the switch of bipolar cell growth, cell fusion during mating and meiosis (Du *et al*, 2016). While the basic principles of the control of the calcium signalling and phosphorylation signalling pathways are understood, little is known about the interplay between these parallel modes of regulation.

We have used molecular cell biological, biochemical and single molecule biophysical techniques to identify and characterise a novel TORC2-Gad8 dependent system regulating calcium-dependent switching of different calmodulin light chain(s) binding to the neck region of Myo1. We define the

contribution that each calmodulin makes to the regulation of this conserved motor protein and describe how they affect the conformation of Myo1 lever arm. We propose that a concerted mode of regulation by calcium and phosphorylation controls motility and function of Myo1 in response to cell cycle progression.

## Results

### *S. pombe* myosin-1 is phosphorylated within the IQ neck domain.

Phospho-proteomic studies of the fission yeast, *S. pombe*, (Carpy *et al*, 2014; Wilson-Grady *et al*, 2008) have revealed a conserved phosphoserine residue located within the IQ motif-containing neck region of class I & V myosins (Figure 1A). The location of this AGC family kinase consensus phosphoserine site (Pearce *et al*, 2010) has the potential to impact myosin activity and function by affecting light chain binding and conformation of the lever arm. We generated polyclonal antibodies that recognised *S. pombe* myosin-1 when phosphorylated at this conserved serine at position 742 ($Myo1^{S742}$). $Myo1^{S742}$ phosphorylation was significantly reduced in cells lacking Ste20 (the fission yeast homologue of the core TORC2 component, RICTOR), and abolished in cells lacking the downstream AGC kinase, Gad8. Thus, $Myo1^{S742}$ is phosphorylated in a TORC2 - Gad8 kinase dependent manner (Figure 1B).

Within cells Gad8 kinase activity is reduced through phosphorylation of a conserved threonine (T6) residue (Du *et al*, 2016; Halova *et al*, 2013) (Figure 1C). A significantly reduction of $Myo1^{S742}$ phosphorylation was observed in cells expressing phospho-mimetic Gad8.T6D (Figure 1D), which has reduced Gad8 kinase activity (Du *et al*, 2016). *S. pombe* cells lacking either TORC2 or Gad8 display defects in actin organisation, regulating polaried growth and control of cell cycle progression (Petersen & Nurse, 2007; Du *et al*, 2016). Similarly, replacing Myo1 serine 742 with a phosphorylation resistant alanine residue in *myo1.S742A* cells blocked cell division when cultured for an extended period in restricted-growth media (mean length ±SEM (μm): wt - 6.67 ± 0.3; *myo1.S742A* - 18.50 ± 1.3 (n>300)) (Figure 1E). Therefore, while Gad8 may not directly phosphorylate $Myo1^{S742}$, phosphorylation of this residue is dependent upon the TORC2-Gad8 signalling pathway.

We conclude that TORC2 directed Gad8 dependent phosphorylation at S742 regulates Myo1 activity.

**Phosphorylation affects Myo1 lever arm structure.**

As serine 742 lies within the IQ motif of the Myo1 neck region, we asked whether Myo1$^{S742}$ phosphorylation alters calmodulin binding and the conformation of the neck region. Isoforms of the $Ca^{2+}$ sensitive fission yeast calmodulin (wild type Cam1 and a Cam1.T6C cysteine mutant, allowing conjugation to a fluorescent probe) were purified, from bacteria co-expressing the fission yeast NatA amino-α-acetyl-transferase complex, in their native amino-terminally (Nt) acetylated forms (Eastwood *et al*, 2017). Two methods were used to measure $Ca^{2+}$-dependent changes in Cam1 conformation. First, a FRET-based sensor was generated consisting of N-terminal CyPet donor and C-terminal, YPet acceptor fluorophores were fused in-frame with Cam1 (Nguyen & Daugherty, 2005) (Figure 2A). Second, Nt-acetylated Cam1.T6C was conjugated to the cysteine-reactive synthetic fluorophore 2-(4'-(iodoacetamido) anilino naphthalene-6-sulfonic acid (IAANS)). As IAANS fluorescence changes in response to changes in its local environment, the fluorescence emission of this fusion will change in response to calcium induced changes in Cam1 conformation. Ca-binding affinity reported by the Cam1-FRET sensor (Figure 2C $pCa_{50}$: 6.12) reflects the global change in Cam1 conformation, while the $Ca^{2+}$-dependent change in IAANS' fluorescence signal (Figure 2C-inset $pCa_{50}$: 6.54) reflects changes in local environment of the amino lobe of Cam1.

Together these probes demonstrated that $Ca^{2+}$ binding induced a change in Cam1 conformation. The rate of $Ca^{2+}$ ion release from Cam1 was independently measured by monitoring changes in fluorescence of the $Ca^{2+}$ indicator Quin-2 (Tsien, 1980). The time-course of $Ca^{2+}$ ion release exhibited three phases; fast, medium and slow of approximately equal amplitude (rate constants 137, 12.9 and 2.0 $s^{-1}$ respectively) indicating the cation has different affinities for each $Ca^{2+}$ binding lobe of Cam1 (Figure 2D).

To characterise Cam1 binding to the IQ neck region of Myo1, recombinant FRET constructs were produced in which CyPet and YPet were separated by

either one, or both, Myo1 IQ motifs (Myo1$^{IQ1}$-FRET, Myo1$^{IQ2}$-FRET, Myo1$^{IQ12}$-FRET) (Figure 2B & Figure 2-figure supplement 1). Cam1 binding to the IQ motif(s) stabilises the α-helix and results in a drop in FRET signal in the absence of calcium (Figure 2E-G). This drop in signal correlates with a Cam1 bound IQ12 neck region length of 4.6 nm (Wu & Brand, 1994), close to the 4.7 nm length predicted from the modelled structure (based upon PDB structure 4R8G). Analysis of interactions between Cam1 and Myo1$^{IQ12}$-FRET revealed two distinct phases to the association of Cam1 molecules with the combined Myo1$^{IQ12}$ motifs. Each phase contributed 50% of the overall change in signal (Figure 2F). The first Cam1-Myo1$^{IQ12}$ binding event corresponded to an affinity of less than 0.1 μM (binding was too tight to calculate affinity with higher precision), while the second event correlated with an approximately 10-fold weaker binding affinity (0.68 μM). This association was sensitive to calcium (pCa of 5.87) (Figure 2C), indicating that Cam1 can only associate with both Myo1 IQ motifs at low cellular $Ca^{2+}$ concentrations. Interestingly while Cam1 bound tightly to a single, isolated, Myo1$^{IQ1}$ alone ($K_d$<0.1 μM), no detectable association was observed for the equivalent single Myo1$^{IQ2}$ motif (Figure 2E). Together these data are consistent with a sequential cooperative binding mechanism by which the stable residency of Cam1 in the first IQ position is required before calmodulin can bind to Myo1$^{IQ2}$.

Replacing serine 742 within the IQ neck region with a phosphomimetic aspartic acid residue had no significant impact upon the affinity, calcium sensitivity or cooperative nature of the interaction between Myo1 and Cam1 (Figure 2F). However, the S742D replacement resulted in a change in maximum FRET signal upon Cam1 binding ($F_{max}$ 46.05 vs 31.64) (Figure 2F), indicating Myo1$^{S742}$ phosphorylation changes the conformation of the lever arm upon Cam1 binding, rather than modulating the affinity for Cam1.

**Phosphorylation regulates Myo1 dynamics and endocytosis.**

Immunofluorescence using Myo1$^{S742}$ phospho-specific antibodies confirmed the presence of serine-742 phosphorylated Myo1 to cortical foci (Figure 3A).

To explore how this phosphorylation affected Myo1 and calmodulin dynamics *in vivo*, we generated prototroph *S. pombe* strains in which endogenous *myo1, cam1, or cam2* genes were fused to cDNA encoding for monomeric fluorescent proteins (Figure 3-figure supplement 1). Using high-speed (20 fps) single molecule TIRF imaging we explored how Myo1$^{S742}$ phosphorylation impacts Myo1 and Cam1 dynamics and function *in vivo*. Myo1 and Cam1 associated with the cell membrane in two distinct ways: we observed both rapid, transient, binding of single Myo1 molecules to the cell membrane, characterised by low-intensity, single, stepwise, changes in intensity (Video 1), alongside longer endocytic events that were much brighter and took much longer (Video 2).

The rapid, single molecule, Myo1 and Cam1 interactions with the membrane had low mobility (0.03 $\mu m^2.s^{-1}$), ~10-times slower than diffusion of integral membrane proteins (Mashanov *et al*, 2010). The individual, diffraction-limited fluorescent spots appeared and disappeared at the cell membrane in a single step. The durations of these short single molecule events (defined as the period over which individual objects were observed and their paths tracked) were exponentially distributed with mean lifetime of ~8 $s^{-1}$ (n = 152) (Video 1). The distribution of the durations of individual Myo1 events is shown in Figure 3-figure supplement 1. In contrast, during endocytic events, the fluorescence signal increased gradually (at a rate corresponding to ~13 molecules.$s^{-1}$), to a peak amplitude corresponding to ~45 molecules of mNeongreen.Myo1, that persisted for ~6 s (plateau phase), before decaying back to baseline level (at a rate of ~14 molecules.$s^{-1}$) (Figure 3B, Video 2). The duration ($T_{dur}$) of endocytic events (measured as described in the Methods) was 13.84 s ± 0.39 (mean ± SEM, n=50) (Figure 3C). While there was significant variation in the maximum mNeongreen.Myo1 intensity (2373 ± 155 AU), there was no correlation between maximum intensity (measured during the plateau phase) and event duration (not shown).

Fluorescence intensity dynamics of Cam1.GFP during endocytic events was

similar to mNeongreen.Myo1, but $T_{dur}$ was significantly shorter (P <0.0001), 10.99 s +/- 0.21 (n=52) while the peak (plateau) intensity was roughly double that measured for mNeongreen.Myo1 and equivalent to ~90 GFP molecules (Figure 3C) consistent with Cam1 occupying both IQ sites within the Myo1 neck region. The briefer event duration observed for Cam1 is best explained by Cam1 dissociating from Myo1 before Myo1 leaves the endocytic patch. This idea was confirmed by two-colour imaging of *mNeongreen.myo1 cam1.mCherry* cells which revealed how Myo1 and Cam1 arrived simultaneously at the endocytic patch before Cam1.mCherry disassociated ~3 s before mNeongreen.Myo1 (Figure 3D, Figure 3-figure supplement 1).

Myo1 and Cam1 dynamics in *myo1.S742A* cells during endocytosis revealed how $Myo1^{S742A}$ had average assembly/disassembly rates and peak intensity measurements that were identical to wild type Myo1, yet the duration of the signal ($T_{dur}$) was 1.5 sec shorter (12.3s +/- 0.31 n=67) (Figure 3E & Figure 3-figure supplement 1). Consistent with the *in vitro* data, the *myo1.S742A* mutation did not impact on the ability of Cam1 molecules to bind both IQ motifs, as average assembly/disassembly rates, and plateau intensity for Cam1 were the same in both wild type and *myo1.S742A* cells. However, $Myo1^{S742A}$ and Cam1 proteins disassociated simultaneously and somewhat earlier during the endocytic event than in otherwise isogenic wild type cells.

**Myo1 S742 is phosphorylated in a cell cycle dependent manner to regulate polarised cell growth**.

Upon cell division, fission yeast cells grow exclusively from the old cell end that existed in the parental cell. At a point during interphase (called New End Take Off -NETO) there is a transition to bipolar growth (Mitchison & Nurse, 1985). This cell cycle switch in growth pattern correlates precisely with a parallel redistribution of endocytic actin patches (Marks & Hyams, 1985).

These TIRF imaging data were consistent with widefield, 3D, time-lapse imaging that showed lifetimes of Myo1 and Cam1 foci were shorter in

*myo1.S742A* cells when compared to *myo1*$^{+}$ (Table 1). In contrast, while the *myo1.S742A* allele did not affect accumulation of Cam2 or LifeACT to sites of endocytosis (Table 1), the rate of endocytosis (measured by actin foci lifetimes) differed significantly ($p < 0.01$) between the old and new ends of *myo1-S742A* cells but not wild type (lifetimes at old end & new cell end: wt 11.96± 2.28 & 11.39±1.07; *myo1.S742A* 14.17±3.3 & 11.09±1.29 sec (mean ± s.d.)). Therefore, while Myo1$^{S742}$ phosphorylation does not impact the assembly of Myo1-Cam1 endocytic foci, it regulates the myosin-1 to modulate the activity and function of the ensemble of endocytic proteins during bipolar growth.

As the *myo1.S742A* allele only affected actin dynamics at the old cell end during bipolar growth we examined whether this post-translational modification was subject to cell cycle dependent variance. Analysis of extracts from cell division cycle mutants arrested in G1 (*cdc10.v50* cells) prior to NETO (Marks *et al*, 1986) or late G2 (*cdc25.22* cells) after NETO, revealed that Myo1$^{S742}$ is phosphorylated in a cell cycle dependent manner (Figure 4A). This was confirmed by monitoring Myo1$^{S742}$ phosphorylation in cells synchronised with respect to cell cycle progression (Figure 4B - D). These data established that at its peak in early interphase (prior to the transition to a bipolar growth pattern), approximately half of cellular Myo1 is phosphorylated on S742, before dropping to undetectable levels by the end of late G2 (the Cdc25 execution point), prior to entry into mitosis. *myo1.S742A* cells have a longer average length compared to wild type (*myo1*$^{+}$: 9.77 ± 1.77 µm; *myo1.S742A*: 13.2 ± 2.47 µm. t-test >99% significance n>500).

In addition to the NETO phenotype, a significant proportion of *myo1.S742A* cells exhibited significant issues with the ability to maintain, linear, polarised, growth, as 24.7% of cells developed a bent morphology (i.e. growth deviates by >5º from longitudinal axis) (Figure 4E - F). The *myo1.S742A* allele did not have an additive effect upon the growth polarity defects associated with cells lacking Tea4, a polarity determinant protein that plays an important role in

integrating actin cytoskeleton function with regulation of polarized cell growth (Martin *et al*, 2005; Tatebe *et al*, 2005) (Figure 5A). Consistently, cell wall staining revealed a significantly higher than normal proportion of *myo1.S742A* cells exhibiting monopolar growth, compared to equivalent wild type, indicating disruption in the switch from monopolar to bipolar growth (Figure 4E - F). This was confirmed by tracking the cellular distribution of the actin patch marker, Sla2/End4, following cell division. Sla2 failed to redistribute to the newly divided end of *myo1.S742A* cells during interphase (Figure 5B). This failure to switch to bipolar growth in *myo1.S742A* cells, as well as restrict growth upon nutrient depletion (Figure 1E), is consistent with the reduced growth rate at the end of log phase and growth to an overall higher density upon reaching stationary phase (Figure 5C).

We conclude that cell cycle dependent changes in Myo1$^{S742}$ phosphorylation modulate the ability of the myosin lever arm region to regulate endocytosis and polarised growth.

**Cam2 associates with internalised endosomes and not Myo1 during vegetative growth.**

Myo1 has been reported to associate with a second calmodulin like protein, Cam2, via its second IQ motif (Sammons *et al*, 2011). However, our data indicate Cam1 occupies both Myo1 IQ motifs during endocytosis. Widefield microscopy revealed Myo1 and Cam1 dynamics (Figure 6A) at endocytic foci differ significantly from Cam2 dynamics. Cam2 is recruited to sites of endocytosis later than Myo1 and Cam1, but prior to vesicle scission/budding, whereupon, like CAPZA$^{Acp1}$, Sla2 and actin, it remains associated with laterally oscillating, internalised, endosomes (Figure 6B-C). Similarly, simultaneous imaging of Cam1 and Cam2 in *cam1.mCherry cam2.gfp* cells revealed how each protein localises to a significant proportion of foci lacking the other calmodulin, to highlight the different timing of engagement of each molecule with the endocytic machinery (Figure 6D). Finally, while Cam1 recruitment to endocytic foci is abolished when Myo1 is absent (Figure 6E),

the intensity, volume and number of Cam2 foci actually increases in the absence of Myo1 (Figure 6F Table 1), even though, internalisation and lateral "oscillating" dynamics of Cam2, and actin were dependent on Myo1 (Figure 6F & G). We assume that this arises from the requirement for prior action of Cam1 for vesicle budding.

TIRF imaging revealed that on average a total of ~30 Cam2 molecules were recruited to each endocytic focus (compared to 45 and 90 molecules observed for Myo1 and Cam1 respectively), and the kinetics of its recruitment to foci differed significantly to that observed for both Myo1 and Cam1. Cam2 signal often increased steadily, before an abrupt decline (Figure 7A), which contrasts with the more gradual (sigmoidal) rise and decay in intensity observed for Myo1 and Cam1 (Figure 3C & E). TIRFM confirmed that Cam2 remained associated with the endocytic vesicles after they were internalised and their connection with the cell membrane was broken (Video 3). Background corrected intensity traces of Cam2 dynamics at the membrane patch before, during, and after the end of endocytosis showed the signal rapidly dropped to baseline (<1s) (Figure 7A), with the Cam2 labelled vesicles remaining visible close to the membrane but moved inwardly, away from the location of the endocytic event. A large number of these mobile, internalised Cam2 labelled vesicles were seen moving within the cytoplasm with relatively low cytosolic background signal (Video 3), indicating that much of the Cam2 was associated with endocytic vesicles and remained bound to mature endosomes. We conclude that endocytosis was inhibited, with Cam2 persisting on the endosome while Myo1 remained at the plasma membrane during and after endosome abscission, as previously reported (Figure 6A, Video 2) (Sirotkin *et al*, 2010; Berro & Pollard, 2014; Picco *et al*, 2015). Thus, whilst Cam1 and Cam2 both localise to sites of endocytosis, they appear to do so at different times, and each have different Myo1 dependencies.

To correlate Myo1-Cam1 dynamics at sites of endocytosis with internalisation of the mature endosome into the cytoplasm, we followed Cam1 and Cam2

dynamics simultaneously in *cam1.mCherry cam2.gfp* cells (Video 4). An average curve (Figure 7B), generated from profiles of 65 two colour individual endocytic events, synchronized relative to $T_{start}$ of Cam1 (see Fig. 3B & C), shows that Cam2 moves away from the cell surface shortly after Cam1 leaves but before Myo1, with the time of abscission ($T_{scis}$) occurring on average 11.4 sec after the event starts ($T_{start}$). Therefore endosome scission takes place immediately prior to the Myo1 disassembly phase (Figure 3B), and around the time Cam1 dissociates from Myo1 (Figure 3C). Intriguingly, while the overall distribution of Myo1 and Cam1 appeared unaffected in *cam2*Δ cells, the number, volume and intensity of foci were significantly reduced (Figure 7C-D Table 1).

**Serine 742 phosphorylation increases the affinity of a single Cam2 for Myo1.**

*In vitro* analysis revealed how two Cam2 molecules can associate with the unphosphorylated $Myo1^{IQ12}$ region (Figure 2F) with 2 distinct phases. In contrast to Cam1 in which the two $Myo1^{IQ12}$ binding events contributed equally to the change in FRET signal, for Cam2 70% of the signal change was brought about by a single binding event, associated with an affinity of 1.10 μM. The smaller amplitude and tighter binding signal is not accurately measurable, but the combined change in signal is consistent with 2 binding events.

As predicted from sequence analysis, Cam2 failed to associate with calcium (Figure 2D), and its conformation and interactions with Myo1 were insensitive to the divalent cation (Figure 2G). Like Cam1, Cam2 had a higher affinity for the first IQ motif (0.4 μM) than for both IQ1 and IQ2 together, and failed to bind IQ2 alone (Figure 2E). Cam1 calcium binding, as measured by IAANS labelling or change in Quin-2 fluorescence were unaffected by Cam2, while gel filtration and fluorescence binding assays provided no evidence of a direct physical interaction between the two proteins (Figure 2-figure supplement 2). Interestingly a difference observed in fluorescence amplitudes between Cam1

and Cam2 binding to the IQ12 motif indicates an impact upon the conformation of the lever arm (Figure 2G), providing a potential mechanism to directly control Myo1 motor activity. However, Myo1$^{S742}$ phosphorylation had no measurable impact upon the dynamics and distribution of Cam2 within *S. pombe* cells undergoing normal vegetative growth (Figure 8A Table 1).

**Cam1 and Cam2 associate with Myo1 during meiosis.**

Calcium levels within log phase yeast cells are relatively low (100-200 nM) (Ma *et al*, 2011; Miseta *et al*, 1999), and so provide favourable conditions for Cam1 to associate with Myo1 (pCa - 5.87). Analysis of cell fluorescence indicated the relative abundance of Myo1 : Cam1 : Cam2 within the *S. pombe* cell to be 0.25 : 1.56 : 1 (Table 1), which is similar to the ratios defined by quantitative proteomic analysis of 0.45 : 1.56 : 1 (Marguerat *et al*, 2012). Similarly, image analysis of Cam1-GFP fluorescence showed how 1.7% of Cam1 associated with discrete foci within cells (Table 1), 40% of which was dependent upon Myo1, with the majority associating with the SPB (Figure 6E). This indicates ~0.68% of cellular Cam1 associates with Myo1 at dynamic endocytic foci. These relative protein levels, binding affinities and low $Ca^{2+}$ concentrations favour Cam1 binding to Myo1, over Cam2 at both IQ sites (Figure 8B), consistent with *in vivo* observations.

While $Ca^{2+}$ levels are low during vegetative growth, sporadic prolonged calcium bursts occur upon pheromone release during mating (Carbó *et al*, 2016; Iida *et al*, 1990), and levels elevate significantly (~10 fold) during the subsequent meiosis and sporulation (Suizu *et al*, 1995). Cam1 would be less likely to bind to Myo1 in these conditions (pCa 5.87). We observed Myo1$^{S742}$ is phosphorylated in mating and meiotic cells (Figure 8C). Cam2 abundance simultaneously increases significantly in relation to Cam1 upon starvation, mating and entry into meiosis (Mata & Bähler, 2006; Mata *et al*, 2002). These conditions favour interactions between Myo1-Cam2 over an association of Cam1 with Myo1 (Figure 8B), which is consistent with both Myo1 and Cam2 playing important roles at the leading edge of forespore membrane formation

during meiosis (Toya *et al*, 2001; Itadani *et al*, 2007). Consistent with this prediction, Myo1, Cam1, Cam2 foci lifetime and dynamics differ significantly to those observed in vegetative cells ($P<0.0001$), lasting significantly longer (>1 min) in meiotic and sporulating cells (Table 1). In contrast to vegetative cells, during meiosis and subsequent spore formation, like Myo1 and Cam1, cortical foci containing accumulations of Cam2 and actin were less dynamic, lacking any oscillation and remaining in a fixed position, with significantly longer lifetime than within actively growing cells (Figure 8D, Table 1, Video 5-8). Consistent with this, endocytosis is significantly diminished in fusing and meiotic cells (Figure 8E) containing the stable Myo1/Cam1/Cam2/actin foci, indicating the the reduction in foci dynamics minimises endocytosis in meiotic cells.

Finally, we used the *myo1.S742A* allele to monitor the impact of Myo1$^{S742}$ phosphorylation on Myo1, Cam1 and Cam2 dynamics during meiosis. In contrast to wild type cells, the lifetime of Myo1 and Cam1 foci were not significantly different to each other in *myo1.S742A* cells. In addition the lifetime of the Myo1 and Cam1 foci in *myo1.S742A* cells were significantly reduced from wild type. Cam2 dynamics did not correlate with Myo1 in *myo1.S742A* cells, which is in contrast to wild type (Table 1). Myo1 and Cam1 foci were also seen to be shorter in *cam2*Δ cells during meiosis, when compared to wild type (Table 1). These data indicate Myo1$^{S742}$ phosphorylation is required for Cam2 to interact with the Myo1 IQ motif and threreby reduce Myo1 foci dynamics.

The majority of Cam2 foci remained present in the cell for greater than 2 mins in meiotic cells lacking Myo1$^{S742}$ phosphorylation. Such timing differs significantly from the dynamics of non-phosphorylatable Myo1$^{S742A}$, indicating normal Cam1 and Cam2 interactions with Myo1 were abolished. Consistent with observations of *myo1.S742A* cells grown to stationary phase (Figure 1E), heterothallic (h$^{90}$) nitrogen starved $G_1$ arrested *myo1.S742A* cells failed to inhibit polar growth (Figure 8F). 27.9% of mating *myo1.S742A* cells continued to grow at their mating (schmooing) tips (*myo1*$^{+}$ 1.8% vs *myo1.S742A* 27.9% cells had long schmoo tips. n>100), and meioses frequently produced asci with an abnormal number of unequally sized spores (Figure 8F arrowheads)

501 (*myo1*$^{+}$ – 0.9%, *myo1.S742A* – 13.1%. n>100). This spore defect phenotype
502 is reminiscent of the meiotic phenotype of *cam2*Δ cells (Itadani *et al*, 2007),
503 which supports the view that an increase in cellular $Ca^{2+}$ and $Myo1^{S742}$
504 phosphorylation are both key for Cam2 association with and regulation of
505 Myo1.

506

507 These data support a model by which changes in calcium levels and TORC2
508 dependent phosphorylation status provides a simple two stage mechanism for
509 modulating motor activity by modifying lever arm conformation as well as
510 switching calmodulin light chain preference in order to co-ordinate myosin
511 function with changing environmental and cell cycle dependent needs of the
512 cell (Figure 8B & F).

## Discussion

Myosins are subject to diverse modes of regulation, including modulation of the composition of the actin track, changes to cargo and light chain interactions, alongside phosphorylation to change core physical properties of the motor. Here we describe a newly discovered mechanism by which phosphorylation of the myosin heavy chain (Figure 1) regulates light chain specificity, lever arm conformation and flexibility, to impact upon cellular function. During the vegetative life cycle, at basal levels of cellular calcium, *S. pombe* Myo1 preferentially associates with two molecules of the calcium regulated calmodulin light chain Cam1 (Figures 2 & 3). During early stages of the cell cycle phosphorylation of the Myo1 neck region (Figure 8G), changes the conformation of the Cam1 associated lever arm to moderate motor activity, and thereby regulate the rate of endocytosis, and a switch from monopolar to bipolar growth (Figure 5).

There is a significant increase in TORC2 and Gad8 activity upon starvation and thereby promote the onset of the meiotic lifecycle (Halova *et al*, 2013; Laboucarié *et al*, 2017; Martín *et al*, 2017). Upon starvation there is an increase in Myo1 serine 472 phosphorylation (Figure 8), and *myo1.S742A* cells fail to arrest growth growth in response to starvation (Figures 1E & 8F). The IQ region phosphorylation, combined with an increase in cytosolic $Ca^{2+}$ levels observed during G1, starvation and meiosis, switches light chain preference to favour recruitment of a single molecule of the calcium insensitive calmodulin like, Cam2. However it is the worth noting that there are currently differences of opinion on the relationship between levels of Gad8 activity and cytosolic calcium (Cohen *et al*, 2014). The structures of the IQ region of Myosin-1 and calmodulin (Lu *et al*, 2014), suggest that phosphorylation of $Myo1^{S742}$ is likely to impact Cam2 binding at the $1^{st}$ IQ position. Furthermore, our data reveals that CaM is unable to associate with IQ2 alone, as occupancy of IQ1 is required before a second CaM can bind to IQ2 (i.e. regulatory cooperative binding). This switch in light chain occupancy may provide a mechanism to change the stiffness of the Myo1 neck region (i.e. the “lever arm”) and thereby modulate the movement and force it

546 produces during the acto-myosin ATPase cycle and/or the load-sensitivity of
547 its actin-bound lifetime.

548

549 While observations within budding yeast indicate that motor activity from a
550 ring of myosins at the lip of the endosome (Mund *et al*, 2018) is necessary for
551 endocytic internalisation, the mechanism by which the myosin interacts with
552 actin to facilitate this localised activation is unknown (Sun *et al*, 2006). Here
553 we find that the size of the early endocytic patch determines the number of
554 Myo1 molecules necessary to generate a critical local concentration of Arp2/3
555 nucleated actin filaments (Barker *et al*, 2007). At the critical concentration
556 myosin heads are able to interact with actin filaments nucleated from either
557 adjacent Myo1 tails or WASP activated Arp2/3 complexes, tethered to the
558 membrane via molecules such as the Talin-like Sla2 (Sirotkin *et al*, 2005;
559 2010). The Myo1 is then primed to act as a tension sensor against the actin
560 filament, as it pushes against the membrane of the internalised endosome,
561 which grows against the significant 0.85 MPa (8.3 atm) turgor pressure within
562 the cell (Minc *et al*, 2009).

563

564 The number of Myo1 molecules at the plasma membrane focus remains
565 constant, as the membrane is internalised, until 2 seconds after Cam1
566 disassociates from Myo1. While the trigger for Cam1 release is unknown, the
567 speed in which the event takes places indicates that it is likely to be initiated
568 by a rapid localised spike in calcium. This could perhaps be driven by a critical
569 level of membrane deformation coupled to calcium influx - similar to
570 processes proposed for mechano-transduction and the role of mammalian
571 myosin-1 within the stereocilia of the inner ear (Adamek *et al*, 2008; Batters
572 *et al*, 2004).

573

574 Once Cam1 detaches from the Myo1 molecule, the neck loses rigidity,
575 reducing tension between the myosin motor and actin filament, to promote
576 detachment from F-actin (Lewis *et al*, 2012; Mentes *et al*, 2018). Given that
577 alone, single molecules of Myo1 do not reside for long at the plasma

membrane (off rate is ~8 $sec^{-1}$ Video 1), without an interaction with actin Myo1 would leave the endocytic patch a second or so after losing its Cam1 light chain . Therefore, after Cam1 release, there is a 2 sec delay in the disappearance of Myo1 signal, as it disassociates from the endocytic machinery (Figure 3C - D).

The conformation and rigidity of the Myo1 lever arm would therefore play a key role in modulating the tension sensing properties of the motor domain. This is consistent with our data, where wild type phosphorylation competent Myo1 resides at the membrane ~1.8 sec longer than Myo1 mutant protein that cannot be phosphorylated at serine 742 ($Myo1^{S742A}$) (Figure 3-figure supplement 1). Phosphorylation-dependent changes in the conformation of the myosin neck provide a simple mechanism to modulate the rate of endocytosis according to the size and needs of the cell. Similarly, in the presence of $Ca^{2+}$ and $Myo1^{S742}$ phosphorylation, a single Cam2 resides at IQ1 motif of the neck (Figure 8B). While bringing about a change in the conformation of the first half of the myosin lever arm (adjacent to the motor domain), the vacant IQ2 motif allows flexibility within the carboxyl half of the neck region. This would provide a relatively tension insensitive motor, that stalls against the actin polymer, and would therefore persist significantly longer at the endocytic foci, as observed to occur here in meiotic cells (Figure 8D, Table 1). These changes in lever arm properties change the overall rate of endocytosis, as observed in differences in the time taken for endosomes to internalise within the cytoplasm (Table 1 & 2).

Thus phosphorylation-dependent changes in the calcium regulated conformation and rigidity of the myosin lever arm could provide a universal mechanism for regulating the diverse cytoplasmic activities and functions of myosin motors within all cells.

## Materials and Methods

**Yeast cell culture:** Cell culture and maintenance were carried out according to (Moreno *et al*, 1991) using Edinburgh minimal medium with Glutamic acid nitrogen source (EMMG) unless specified otherwise. Cells were cultured at 25 ºC unless stated otherwise and cells were maintained as early to mid-log phase cultures for 48 hours before being used for analyses. Genetic crosses were undertaken on MSA plates (Egel *et al*, 1994). All strains used in this study were prototroph and listed in Supplementary File 1.

**Molecular Biology:** *cam1*$^{+}$ (SPAC3A12.14), *cam1.T6C* and *cam2*$^{+}$ (SPAC29A4.05) genes were amplified as *Nde1 - BamH1* fragments from genomic *S. pombe* DNA using o226/o227 and o393/o394 primers and cloned into pGEM-T-Easy (*Promega*, Madison, WI, USA). After sequencing the subsequent genes were cloned into pJC20 (Clos et al., 1990) to generate bacterial calmodulin expression constructs. DNA encoding for the FRET optimized fluorophores CyPet and YPet (Nguyen and Daugherty, 2005) were each amplified using primers o405 / o406 and o403 / o404 respectively. o406 also incorporated DNA at the 3' end of the CyPet ORF encoding for the first IQ motif of the Myo1 neck region, while o404 included DNA encoding a Gly3His6 tag at the 3' of the YPet ORF. The two DNA fragments were cloned into pGEM-T-Easy in a three-way ligation reaction to generate pGEM-CyPet-Myo1IQ1-YPet. The CyPet-Myo1$^{IQ1}$-YPet DNA was subsequently sequencing and cloned as a Nde1 - BamH1 fragment into pJC20 (Clos & Brandau, 1994) to generate pJC20CyPet-Myo1$^{IQ1}$-YPet. Complementary oligonucleotides o425 & o426 were annealed together and ligated into BglII – Xho1 cut pJC20CyPet-Myo1$^{IQ1}$-YPet to generate pJC20CyPet-Myo1$^{IQ12}$-YPet. Similarly, complementary oligonucleotides o429 & o430 were annealed together and subsequently ligated into Sal1-BglII cut pJC20CyPet-Myo1$^{IQ1}$-YPet and the subsequent Xho1 fragment was excised to generate pJC20CyPet-Myo1$^{IQ2}$-YPet. Site directed mutagenesis was carried out using pJC20CyPet-Myo1$^{IQ12}$-YPet template and o427 & o428 primers to generate pJC20CyPet-Myo1$^{IQ12}$S742D-YPet. Complementary oligonucleotides o449 & o450 were annealed together and ligated into Nru1 – Xho1 digested pJC20CyPet-Myo1$^{IQ12}$S742D-YPet to generate pJC20CyPet-Myo1$^{IQ12}$S742A-YPet. All

plasmids were sequenced upon construction. Strains with fluorophore tagged alleles of *cam1*$^{+}$ and *cam2*$^{+}$ were generated as described previously using appropriate template and primers (Bähler *et al*, 1998). Strains in which the *myo1.S742A*, *myo1.S742D*, *mNeongreen-myo1*, *mNeongreen-myo1.S742A*, or *mNeongreen-myo1.S742D* alleles replaced the endogenous *myo1*$^{+}$ gene (SPBC146.13c) were generated using a marker switching method (MacIver *et al*, 2003). Oligonucleotides are described in Supplementary File 2.

**Protein expression & purification:** All recombinant proteins were expressed and purified from BL21 DE3 *E. coli* cells, except Cam1 proteins where BL21 DE3 pNatA cells (Eastwood *et al*, 2017) were used to allow amino-terminal acetylation (Figure 2-figure supplement 1). *Calmodulin purification*: Cell lysates were resuspended in Buffer A (50 mM Tris, 2 mM EDTA, 1 mM DTT, 0.1 mM PMSF, pH 7.5) and precleared by high speed centrifugation (48,500 RCF; 30 min; 4 °C), before ammonium sulphate was added to the supernatant at 35 % saturation, incubated for 30 minutes at 4 °C. Precipitated proteins were removed by centrifugation (48,500 RCF; 30 min; 4 °C). For Cam1 purifications the precipitation cleared supernatant was added to a pre-equilibrated 10 ml phenyl sepharose (CL-4B) column (Buffer B: 50 mM Tris, 1 mM DTT, 1 mM $NaN_3$, 5 mM $CaCl_2$, pH 8.0), washed in 4 volumes of Buffer B before eluted as fractions in Buffer C (50 mM Tris, 1 mM DTT, 1 mM $NaN_3$, 5 mM EGTA, pH 8.0). For Cam2 purification the precipitation cleared supernatant underwent a second round of ammonium sulphate precipitation and clearing, and the subsequent supernatant subjected to isoelectric precipitation (pH 4.3) and centrifugation (48,500 RCF: 30 minutes; 4 °C). The resultant pellet was resuspended in Buffer A, heated to 80 °C for 5 minutes and denatured proteins removed by centrifugation (16,000 RCF; 5 min). *His-tagged* proteins were purified in native conditions using prepacked, pre-equilibrated 5ml $Ni^{2+}$ columns.

**Immunological techniques**: Standard immunological methods were used as described (Harlow & Lane, 1988) . Serine 742 phosphorylation-state specific anti-Myo1 antibodies were raised against phosphate-conjugated peptide encompassing Myo1 serine 742 in SPF rabbits (Eurogentec, Seraing, Belgium), which were subsequently affinity-purified.

673 **Analysis of yeast extracts:** Protein extracts were prepared and analysed as
674 described elsewhere (Baker *et al*, 2016). For western blot analysis anti-Myo1
675 sera was diluted 1:1000, while Myo1 serine 742 phosphorylation state specific
676 antibodies were used at a dilution of 1:50. Gel densitometry was undertaken
677 using ImageJ software.
678 **Fast reaction kinetics:** All transient kinetics were carried out using a HiTech
679 Scientific DF-61 DX2 Stopped Flow apparatus (TgK Scientific, Bradford-upon-
680 Avon, UK) at 20ºC. All data was acquired as the average of 3-5 consecutive
681 shots and analysed using the KineticStudio software supplied with the
682 equipment. Quin-2 fluorescence was excited at 333 nm and used a Schott
683 GG445 cut off filter to monitor fluorescence above 445 nm. IAANS (2-(4'-
684 (iodoacetamido)anilino)-naphthalene-6-sulfonic acid) was excited at 335 nm
685 and fluorescence was monitored through a GG455 filter. For the FRET
686 measurements, CyPet was excited at 435 nm and YPet emission was
687 monitored through a combination of a Wrattan Gelatin No12 (Kodak) with a
688 Schott GG495 nm filter to monitor fluorescence at 525-530 nm.
689 **Fluorescence spectra:** Emission spectra were obtained using a Varian Cary
690 Eclipse Fluorescence Spectrophotometer (Agilent Technologies, Santa Clara,
691 CA) using a 100 µl Quartz cuvette. For FRET measurements samples were
692 excited at 435 nm (CyPet excitation) and emission was monitored from 450 –
693 600 nm with both slits set to 1 nm. Affinity experiments were carried out using
694 1 µM IQ-FRET protein with varying concentrations of Cam1 or Cam2 in a final
695 volume of 100 µl in analysis buffer of 140 mM KCl, 20 mM MOPS, pH 7.0 with
696 or without 2 mM $MgCl_2$ and with 2 mM of EGTA, $CaCl_2$ or $Ca^{2+}$-EGTA as
697 required. Distances between FRET fluorophores were calculated as described
698 previously (Wu & Brand, 1994) using an CyPet-YPet $R_0$ value of 53.01.
699 **Live cell imaging:** Live cell widefield fluorescence imaging was undertaken
700 as described previously (Baker *et al*, 2016). For Total Internal Reflection
701 Fluorescence Microscopy (TIRFM) *S. pombe* cells were immobilized on №1,
702 Ø 25 mm lectin coated coverslips and placed into imaging chambers filled
703 with EMMG medium. A previously described custom TIRF Microscope
704 (Mashanov *et al*, 2003) was used to image individual cells at a rate of 20 fps
705 in either single of dual colour mode. Lasers: 488 nm/100 mW and 561 nm/150

mW (*Omicron*, Germany); emission filters 525/50 nm and 585/29 nm, dichroic mirror 552 nm (*Semrock*, NY); all lenses and mirrors (*Thorlabs*, NJ), except two Ø3 mm mirrors (*Comar Optics*, UK) which directed light in and out of the 100× 1.45 NA objective lens (*Olympus*, Japan). Sequences of images were captured using one or two iXon897BV cameras (*Andor Technology*, UK) with custom made acquisition software. 100% laser power (488 nm) was used to image individual mNeongreen-Myo1 and Cam1-GFP molecules. The laser intensity was reduced to 20% during endocytosis imaging experiments to minimize photobleaching. All imaging was undertaken at 23 °C.

**Immunofluorescence:** Immunofluorescence microscopy was performed as described previously (Hagan & Hyams, 1988), except gluteraldehyde was omitted. Images were captured using the above widefield imaging system. Anti-Myo1 sera (Attanapola *et al*, 2009) were used at a dilution of 1:100, while affinity purified Myo1 serine 742 phosphorylation state specific antibodies were used at a dilution of 1:10.

**Image analysis:** *Widefield data* was analysed using Autoquant software (*MediaCybernetics*, Rockville, MD, USA). All 3d image stacks were subjected to blind 3d deconvolution before analysis. Average size and number and cellular distribution of foci were calculated from all foci present within ≥ 30 cells for each sample examined. Timing of foci events were calculated from kymographs generated in Metamorph software (*Molecular Devices*, Sunnyvale, CA, USA). The proportion of cells displaying a bent cell phenotype was determined from more than >350 calcofluor (1 $mg.ml^{-1}$) stained cells for each strain. Bent cells were defined by a deviation in the direction of growth of > 5º from the longitudinal axis. *TIRF data* analyses, including single molecule detection and tracking, was undertaken using GMimPro software (Mashanov & Molloy, 2007). Endocytic events were identified by creating an image representing the standard deviation of each pixel over the whole video sequence (known as a “z-projection”). Bright spots in this image correspond to regions of the yeast cell that showed large intensity fluctuations associated with endocytic activity. Intensity trajectories in these regions of interest (ROIs) (0.5 µm diameter, 5x5 pixels) were saved for future analysis. To correct for local variation in background signal, the average intensity in a region 1.5 µm

diameter around the endocytosis site (but not including the central ROI) was subtracted. Data from ROIs that were contaminated by other endocytosis events, occurring in close proximity and close in time, were manually excluded from the analysis. It was critical to identify accurately the start and end of each endocytosis event so that individual traces could be averaged. To facilitate this, the rising and falling phases of the intensity trace were fitted with a straight line (60 data points, 3 sec duration), see Figure 3C for example. The intercept of this line with the baseline intensity gave the $t_{start}$ and $t_{end}$ values and event duration ($T_{dur} = T_{end} - T_{start}$) (see Figure 7A). The amplitude (intensity) of the event $A_{av}$ was measured at the middle of the event by averaging 60 data points from $5^{th}$ to $8^{th}$ second from the $T_{start}$, grey bar on Figure 3B. Intensity traces for each given condition were synchronised to the starting point ($T_{start}$) and averaged (except Cam2-GFP traces which were synchronised using $t_{start}$ measured from simultaneously acquired Cam1-mCherry signal). Similarly, traces were synchronised to their end point ($T_{end}$) and averaged. The mean duration of the events ($T_{dur}$) for each condition was then used to reconstruct the mean intensity changes with calculated errors for event amplitude and timing (Table 2). We used the results of single molecule imaging experiments to calculate the number of single fluorescent molecules contributing to the spot intensity at a given time. Since the falling and rising phases of most events fitted well to a simple linear equation, the *slope* of the fitted lines was used to estimate the rate of accumulation and dissociation of the fluorescent molecules (Figure 3C). As Cam2-GFP remained bound to the endocytic vesicle, when vesicle scission occurred intensity fell rapidly to zero as the vesicle diffused from the TIRF evanescent field; the time of scission was defined as $T_{scis}$ (Figure 7A). Single particle tracking was performed using GMimPro (Mashanov & Molloy, 2007) (ASPT module) so that the paths (or trajectories) of individual Myo1 molecules bound to cell membrane could be traced. Trajectories were analysed to yield mean intensities for individual mNeonGreen and eGFP labelled proteins, which could be used to estimate the number of fluorescently-tagged molecules associated with each endocytotic event. Intensity-versus-time plots were generated from averages of >30 foci for each protein in each genetic background examined.

**Acknowledgements**

We thank M. Balasubramanian, I. Hagan, P. Nurse, C. Shimoda and T. Pollard for strains; Ben Goult, Iain Hagan and Janni Petersen for stimulating discussions and comments on the manuscript. This work was supported by the University of Kent and funding from the Biotechnology and Biological Sciences Research Council (BB/J012793/1 & BB/M015130/1), a Royal Society Industry Fellowship to DPM; a CASE industrial bursary from Cairn Research Ltd to KB and by the Francis Crick Institute which receives core funding from Cancer Research UK (FC001119), the UK Medical Research Council (FC001119) and the Wellcome Trust (FC001119) GIM and JEM.

## References


Adamek N, Coluccio LM & Geeves MA (2008) Calcium sensitivity of the cross-bridge cycle of Myo1c, the adaptation motor in the inner ear. *Proceedings of the National Academy of Sciences* **105:** 5710–5715

Attanapola SL, Alexander CJ & Mulvihill DP (2009) Ste20-kinase-dependent TEDS-site phosphorylation modulates the dynamic localisation and endocytic function of the fission yeast class I myosin, Myo1. *J. Cell. Sci.* **122:** 3856–3861

Baker K, Kirkham S, Hálová L, Atkin J, Franz-Wachtel M, Cobley D, Krug K, Macek B, Mulvihill DP & Petersen J (2016) TOR complex 2 localises to the cytokinetic actomyosin ring and controls the fidelity of cytokinesis. *J. Cell. Sci.* **129:** 2613–2624

Barker SL, Lee L, Pierce BD, Maldonado-Báez L, Drubin DG & Wendland B (2007) Interaction of the endocytic scaffold protein Pan1 with the type I myosins contributes to the late stages of endocytosis. *Molecular Biology of the Cell* **18:** 2893–2903

Batters C, Arthur CP, Lin A, Porter J, Geeves MA, Milligan RA, Molloy JE & Coluccio LM (2004) Myo1c is designed for the adaptation response in the inner ear. *EMBO J.* **23:** 1433–1440

Bähler J, Wu JQ, Longtine MS, Shah NG, McKenzie A, Steever AB, Wach A, Philippsen P & Pringle JR (1998) Heterologous modules for efficient and versatile PCR-based gene targeting in Schizosaccharomyces pombe. *Yeast* **14:** 943–951

Bement WM & Mooseker MS (1995) TEDS rule: a molecular rationale for differential regulation of myosins by phosphorylation of the heavy chain head. *Cell Motil. Cytoskeleton* **31:** 87–92

Berro J & Pollard TD (2014) Local and global analysis of endocytic patch dynamics in fission yeast using a new ‘temporal superresolution’ realignment method. *Molecular Biology of the Cell* **25:** 3501–3514

Carbó N, Tarkowski N, Ipiña EP, Dawson SP & Aguilar PS (2016) Sexual pheromone modulates the frequency of cytosolic Ca2+ bursts in Saccharomyces cerevisiae. *Molecular Biology of the Cell* **28:** 501–510

Carpy A, Krug K, Graf S, Koch A, Popic S, Hauf S & Macek B (2014) Absolute proteome and phosphoproteome dynamics during the cell cycle of Schizosaccharomyces pombe (Fission Yeast). *Mol. Cell Proteomics* **13:** 1925–1936

Clos J & Brandau S (1994) pJC20 and pJC40--two high-copy-number vectors for T7 RNA polymerase-dependent expression of recombinant genes in Escherichia coli. *Protein Expression and Purification* **5:** 133–137

825 Cohen A, Kupiec M & Weisman R (2014) Glucose activates TORC2-Gad8
826 protein via positive regulation of the cAMP/cAMP-dependent protein
827 kinase A (PKA) pathway and negative regulation of the Pmk1 protein-
828 mitogen-activated protein kinase pathway. *J. Biol. Chem.* **289:** 21727–
829 21737

830 Crivici A & Ikura M (1995) Molecular and structural basis of target recognition
831 by calmodulin. *Annu Rev Biophys Biomol Struct* **24:** 85–116

832 Du W, Forte GM, Smith D & Petersen J (2016) Phosphorylation of the amino-
833 terminus of the AGC kinase Gad8 prevents its interaction with TORC2.
834 *Open Biology* **6:** 150189

835 Eastwood TA, Baker K, Brooker HR, Frank S & Mulvihill DP (2017) An
836 enhanced recombinant amino-terminal acetylation system and novel in
837 vivohigh-throughput screen for molecules affecting α-synuclein
838 oligomerisation. *FEBS Letters* **106:** 8157–9

839 Egel R, Willer M, Kjaerulff S, Davey J & Nielsen O (1994) Assessment of
840 pheromone production and response in fission yeast by a halo test of
841 induced sporulation. *Yeast* **10:** 1347–1354

842 Hagan IM & Hyams JS (1988) The use of cell division cycle mutants to
843 investigate the control of microtubule distribution in the fission yeast
844 Schizosaccharomyces pombe. *J. Cell. Sci.* **89 ( Pt 3):** 343–357

845 Halova L, Du W, Kirkham S, Smith DL & Petersen J (2013) Phosphorylation of
846 the TOR ATP binding domain by AGC kinase constitutes a novel mode of
847 TOR inhibition. *The Journal of Cell Biology* **203:** 595–604

848 Harlow ED & Lane D (1988) Antibodies: a laboratory manual New York: Cold
849 Spring Harbour Laboratory Press,

850 Hartmuth S & Petersen J (2009) Fission yeast Tor1 functions as part of
851 TORC1 to control mitotic entry through the stress MAPK pathway
852 following nutrient stress. *J. Cell. Sci.* **122:** 1737–1746

853 Heissler SM & Sellers JR (2016a) Various Themes of Myosin Regulation.
854 *Journal of Molecular Biology* **428:** 1927–1946

855 Heissler SM & Sellers JR (2016b) Kinetic Adaptations of Myosins for Their
856 Diverse Cellular Functions. *Traffic* **17:** 839–859

857 Iida H, Yagawa Y & Anraku Y (1990) Essential role for induced Ca2+ influx
858 followed by [Ca2+]i rise in maintaining viability of yeast cells late in the
859 mating pheromone response pathway. A study of [Ca2+]i in single
860 Saccharomyces cerevisiae cells with imaging of fura-2. *J. Biol. Chem.*
861 **265:** 13391–13399

862 Itadani A, Nakamura T & Shimoda C (2007) Localization of type I myosin and
863 F-actin to the leading edge region of the forespore membrane in
864 Schizosaccharomyces pombe. *Cell Struct. Funct.* **31:** 181–195

865 Itadani A, Nakamura T, Hirata A & Shimoda C (2010) Schizosaccharomyces
866 pombe Calmodulin, Cam1, Plays a Crucial Role in Sporulation by
867 Recruiting and Stabilizing the Spindle Pole Body Components
868 Responsible for Assembly of the Forespore Membrane. *Eukaryotic Cell* **9:**
869 1925–1935

870 Jacinto E, Loewith R, Schmidt A, Lin S, Rüegg MA, Hall A & Hall MN (2004)
871 Mammalian TOR complex 2 controls the actin cytoskeleton and is
872 rapamycin insensitive. *Nat. Cell Biol.* **6:** 1122–1128

873 Kendrick-Jones J, Smith RC, Craig R & Citi S (1987) Polymerization of
874 vertebrate non-muscle and smooth muscle myosins. *Journal of Molecular*
875 *Biology* **198:** 241–252

876 Laboucarié T, Detilleux D, Rodriguez Mias RA, Faux C, Romeo Y, Franz-
877 Wachtel M, Krug K, Macek B, Villén J, Petersen J & Helmlinger D (2017)
878 TORC1 and TORC2 converge to regulate the SAGA co-activator in
879 response to nutrient availability. *EMBO Rep* **18:** 2197–2218

880 Laplante M & Sabatini DM (2012) mTOR signaling in growth control and
881 disease. *Cell* **149:** 274–293

882 Lee S, Comer FI, Sasaki A, McLeod IX, Duong Y, Okumura K, Yates JR III,
883 Parent CA & Firtel RA (2005) TOR Complex 2 Integrates Cell Movement
884 during Chemotaxis and Signal Relay in Dictyostelium. *Molecular Biology*
885 *of the Cell* **16:** 4572–4583

886 Lee WL, Bezanilla M & Pollard TD (2000) Fission yeast myosin-I, Myo1p,
887 stimulates actin assembly by Arp2/3 complex and shares functions with
888 WASp. *The Journal of Cell Biology* **151:** 789–800

889 Lewis JH, Greenberg MJ, Laakso JM, Shuman H & Ostap EM (2012) Calcium
890 regulation of Myosin-I tension sensing. *Biophysical Journal* **102:** 2799–
891 2807

892 Liu L & Parent CA (2011) Review series: TOR kinase complexes and cell
893 migration. *The Journal of Cell Biology* **194:** 815–824

894 Lu Q, Li J, Ye F & Zhang M (2014) Structure of myosin-1c tail bound to
895 calmodulin provides insights into calcium-mediated conformational
896 coupling. *Nat Struct Mol Biol* **22:** 81–88

897 Ma Y, Sugiura R, Koike A, Ebina H, Sio SO & Kuno T (2011) Transient
898 Receptor Potential (TRP) and Cch1-Yam8 Channels Play Key Roles in
899 the Regulation of Cytoplasmic Ca2+ in Fission Yeast. *PLoS ONE* **6:**
900 e22421

901 MacIver FH, Glover DM & Hagan IM (2003) A 'marker switch' approach for
902 targeted mutagenesis of genes in Schizosaccharomyces pombe. *Yeast*
903 **20:** 587–594

Marguerat S, Schmidt A, Codlin S, Chen W, Aebersold R & Bähler J (2012) Quantitative analysis of fission yeast transcriptomes and proteomes in proliferating and quiescent cells. *Cell* **151:** 671–683

Marks J & Hyams JS (1985) Localization of F-actin through the cell division cycle of Schizosaccharomyces pombe. *European Journal of Cell Biology* **39:** 27–32

Marks J, Hagan IM & Hyams JS (1986) Growth polarity and cytokinesis in fission yeast: the role of the cytoskeleton. *J. Cell Sci. Suppl.* **5:** 229–241

Martin SG, McDonald WH, Yates JR III & Chang F (2005) Tea4p Links Microtubule Plus Ends with the Formin For3p in the Establishment of Cell Polarity. *Developmental Cell* **8:** 479–491

Martín R, Portantier M, Chica N, Nyquist-Andersen M, Mata J & Lopez-Aviles S (2017) A PP2A-B55-Mediated Crosstalk between TORC1 and TORC2 Regulates the Differentiation Response in Fission Yeast. *Curr. Biol.* **27:** 175–188

Mashanov GI & Molloy JE (2007) Automatic detection of single fluorophores in live cells. *Biophysj* **92:** 2199–2211

Mashanov GI, Nobles M, Harmer SC, Molloy JE & Tinker A (2010) Direct observation of individual KCNQ1 potassium channels reveals their distinctive diffusive behavior. *J. Biol. Chem.* **285:** 3664–3675

Mashanov GI, Tacon D, Knight AE, Peckham M & Molloy JE (2003) Visualizing single molecules inside living cells using total internal reflection fluorescence microscopy. **29:** 142–152

Mata J & Bähler J (2006) Global roles of Ste11p, cell type, and pheromone in the control of gene expression during early sexual differentiation in fission yeast. *Proc. Natl. Acad. Sci. U.S.A.* **103:** 15517–15522

Mata J, Lyne R, Burns G & Bähler J (2002) The transcriptional program of meiosis and sporulation in fission yeast. *Nat Genet* **32:** 143–147

Mentes A, Huehn A, Liu X, Zwolak A, Dominguez R, Shuman H, Ostap EM & Sindelar CV (2018) High-resolution cryo-EM structures of actin-bound myosin states reveal the mechanism of myosin force sensing. *Proceedings of the National Academy of Sciences* **115:** 1292–1297

Minc N, Boudaoud A & Chang F (2009) Mechanical forces of fission yeast growth. *Curr. Biol.* **19:** 1096–1101

Miseta A, Fu L, Kellermayer R, Buckley J & Bedwell DM (1999) The Golgi apparatus plays a significant role in the maintenance of Ca2+ homeostasis in the vps33Delta vacuolar biogenesis mutant of Saccharomyces cerevisiae. *J. Biol. Chem.* **274:** 5939–5947

942 Mitchison JM & Nurse P (1985) Growth in cell length in the fission yeast
943 Schizosaccharomyces pombe. *J. Cell. Sci.* **75:** 357–376

944 Moreno S, Klar A & Nurse P (1991) Molecular genetic analysis of fission yeast
945 Schizosaccharomyces pombe. *Meth. Enzymol.* **194:** 795–823

946 Moser MJ, Flory MR & Davis TN (1997) Calmodulin localizes to the spindle
947 pole body of Schizosaccharomyces pombe and performs an essential
948 function in chromosome segregation. *J. Cell. Sci.* **110 ( Pt 15):** 1805–1812

949 Moser MJ, Lee SY, Klevit RE & Davis TN (1995) Ca2+ binding to calmodulin
950 and its role in Schizosaccharomyces pombe as revealed by mutagenesis
951 and NMR spectroscopy. *J. Biol. Chem.* **270:** 20643–20652

952 Mund M, van der Beek JA, Deschamps J, Dmitrieff S, Hoess P, Monster JL,
953 Picco A, Nedelec F, Kaksonen M & Ries J (2018) Systematic Nanoscale
954 Analysis of Endocytosis Links Efficient Vesicle Formation to Patterned
955 Actin Nucleation. *Cell* **174:** 1–13

956 Nguyen AW & Daugherty PS (2005) Evolutionary optimization of fluorescent
957 proteins for intracellular FRET. *Nat Biotechnol* **23:** 355–360

958 O'Connell CB, Tyska MJ & Mooseker MS (2007) Myosin at work: motor
959 adaptations for a variety of cellular functions. *Biochim. Biophys. Acta*
960 **1773:** 615–630

961 Pasapera AM, Plotnikov SV, Fischer RS, Case LB, Egelhoff TT & Waterman
962 CM (2015) Rac1-dependent phosphorylation and focal adhesion
963 recruitment of myosin IIA regulates migration and mechanosensing. *Curr.*
964 *Biol.* **25:** 175–186

965 Pearce LR, Komander D & Alessi DR (2010) The nuts and bolts of AGC
966 protein kinases. *Nat Rev Mol Cell Biol* **11:** 9–22

967 Petersen J & Nurse P (2007) TOR signalling regulates mitotic commitment
968 through the stress MAP kinase pathway and the Polo and Cdc2 kinases.
969 *Nature Publishing Group* **9:** 1263–1272

970 Picco A, Mund M, Ries J, Nedelec F & Kaksonen M (2015) Visualizing the
971 functional architecture of the endocytic machinery. *eLife* **4:**

972 Redowicz MJ (2001) Regulation of nonmuscle myosins by heavy chain
973 phosphorylation. *J. Muscle Res. Cell. Motil.* **22:** 163–173

974 Rogers SL, Karcher RL, Roland JT, Minin AA, Steffen W & Gelfand VI (1999)
975 Regulation of melanosome movement in the cell cycle by reversible
976 association with myosin V. *The Journal of Cell Biology* **146:** 1265–1276

977 Sammons MR, James ML, Clayton JE, Sladewski TE, Sirotkin V & Lord M
978 (2011) A calmodulin-related light chain from fission yeast that functions
979 with myosin-I and PI 4-kinase. *J. Cell. Sci.* **124:** 2466–2477

980 Sirotkin V, Beltzner CC, Marchand J-B & Pollard TD (2005) Interactions of
981 WASp, myosin-I, and verprolin with Arp2/3 complex during actin patch
982 assembly in fission yeast. *The Journal of Cell Biology* **170:** 637–648

983 Sirotkin V, Berro J, Macmillan K, Zhao L & Pollard TD (2010) Quantitative
984 analysis of the mechanism of endocytic actin patch assembly and
985 disassembly in fission yeast. *Molecular Biology of the Cell* **21:** 2894–2904

986 Suizu T, Tsutsumi H, Kawado A, Suginami K, Imayasu S & Murata K (1995)
987 Calcium ion influx during sporulation in the yeast Saccharomyces
988 cerevisiae. *Can. J. Microbiol.* **41:** 1035–1037

989 Sun Y, Martin AC & Drubin DG (2006) Endocytic Internalization in Budding
990 Yeast Requires Coordinated Actin Nucleation and Myosin Motor Activity.
991 *Developmental Cell* **11:** 33–46

992 Takeda T & Yamamoto M (1987) Analysis and in vivo disruption of the gene
993 coding for calmodulin in Schizosaccharomyces pombe. *Proc. Natl. Acad.*
994 *Sci. U.S.A.* **84:** 3580–3584

995 Tatebe H, Shimada K, Uzawa S, Morigasaki S & Shiozaki K (2005)
996 Wsh3/Tea4 Is a Novel Cell-End Factor Essential for Bipolar Distribution of
997 Tea1 and Protects Cell Polarity under Environmental Stress in S. pombe.
998 *Current Biology* **15:** 1006–1015

999 Toya M, Motegi F, Nakano K, Mabuchi I & Yamamoto M (2001) Identification
1000 and functional analysis of the gene for type I myosin in fission yeast.
1001 *Genes Cells* **6:** 187–199

1002 Trybus KM, Gushchin MI, Lui H, Hazelwood L, Krementsova EB, Volkmann N
1003 & Hanein D (2007) Effect of calcium on calmodulin bound to the IQ motifs
1004 of myosin V. *J. Biol. Chem.* **282:** 23316–23325

1005 Tsien RY (1980) New calcium indicators and buffers with high selectivity
1006 against magnesium and protons: design, synthesis, and properties of
1007 prototype structures. *Biochemistry* **19:** 2396–2404

1008 Wilson-Grady JT, Villén J & Gygi SP (2008) Phosphoproteome analysis of
1009 fission yeast. *J. Proteome Res.* **7:** 1088–1097

1010 Win TZ, Mulvihill DP & Hyams JS (2002) Take five: a myosin class act in
1011 fission yeast. *Cell Motil. Cytoskeleton* **51:** 53–56

1012 Wu PG & Brand L (1994) Resonance Energy-Transfer - Methods and
1013 Applications. *Anal. Biochem.* **218:** 1–13

1014

## Figure Legends

**Figure 1. Myo1 serine 742 phosphorylation is TORC2 dependent.** (A) Anti- (A) Sequence alignment of myosin IQ regions highlights an AGC kinase consensus sequence, conserved in class I and V myosins. Underlined residues mark residues within IQ motifs. (B) Western blots of extracts from *myo1*$^{+}$, *myo1-S742A*, *gad8*Δ and *ste20*Δ cells probed with phospho-specific anti-Myo1$^{S742}$ (upper panel) and anti-Myo1 (lower panel) antibodies demonstrate antigen specificity and a Myo1$^{S742}$ phosphorylation state dependence upon the TORC2-Gad8 pathway. Ponceau staining was used to monitor equal loading. Relative Myo1$^{S742}$ phosphorylation levels were calculated from 5 independent equivalent experiments (mean ± sd). (C) A schematic of the TORC2-Gad8 signalling pathway. (D) Myo1$^{S742}$ phosphorylation is reduced in *gad8.T6D* cells, which have reduced Gad8 kinase activity. Relative Myo1$^{S742}$ phosphorylation levels were calculated from 3 independent equivalent experiments (mean ± sd). (E) Nitrogen starved WT and *myo1.S742A* cells. In contrast to WT in which growth arrests, *myo1.S742A* cells continue to growing upon nitrogen starvation induced G1 arrest. Scale – 5 μm.

**Figure 2. *In vitro* characterisation of interactions between Myo1 and Cam1.** (A) Predicted models of the CyPet-Cam1-YPet FRET reporter protein (Cam1-FRET) in the absence (upper panel) and presence (lower panel) of $Ca^{2+}$. (B) Predicted models of the CyPet-Myo1$^{IQ12}$-YPet FRET reporter protein (Myo1IQ12-FRET) in the absence (upper panel) or presence (lower panel) of Calmodulin binding (Cypet – cyan; Cam1 – yellow; YPet – green; IQ domain - magenta). (C) pCa curve plotting $Ca^{2+}$ dependent changes in acceptor fluorescence (plotted as ΔYPet signal) of Cam1-FRET protein (red), Cam1 association with Myo1$^{IQ12}$-FRET (black) and change in fluorescence of IAANS labelled Cam1-T6C (inset). (D) Transient curves of changes in Quin2 fluorescence induced by $Ca^{2+}$ release from Cam1 (red) with 3 exponential fit best fit (black) and Cam2 (blue) illustrate only Cam1 associates with $Ca^{2+}$. (E) Curves plotting Cam1 (black) and Cam2 (red) dependent changes of FRET donor signal of Myo1-FRET proteins containing single IQ domains (IQ1 –

empty shapes; IQ2 – filled shapes) show each CaM associates with IQ1 but not to an equivalent single IQ2 motif region. (F) Curves plotting Cam1 (squares and triangles) and Cam2 (circles and lozenge) dependent changes of FRET donor signal of either 0.5 μM wild type (black & red) or S742D phosphomimetic (blue) Myo1$^{IQ12}$-FRET proteins show while phosphorylation does not significantly impact Cam1 binding, it results in a ~50% drop in Cam2 interaction. (G) Spectra of 0.5 μM Myo1$^{IQ12}$-FRET reporter alone (grey line), or mixed with 10 μM saturating concentrations of: Cam1 + $Ca^{2+}$ (black dotted line), Cam1 - $Ca^{2+}$ (black solid line), Cam2 + $Ca^{2+}$ (red dotted line), or Cam1 - $Ca^{2+}$ (red solid line).

**Figure 3. Myo1 and Cam1 dynamics in wild type and *myo1.S742A* cells.** (A) Maximum projections from 31-z stack widefield immunofluorescence images of wild-type cells probed with anti-Myo1 (left panel) or anti-Myo1$^{S742*}$ phosphospecific (right panels) antibodies illustrate S742 phosphorylated Myo1 localises to endocytic foci (Scale - 5 μm). (B) An example relative intensity trace of a single mNeongreen.Myo1 endocytic event. Linear fitting (grey lines, 60 points) was used to find the maximum gradient for both rising and falling slopes. The intercept with zero intensity level was used to calculate $T_{start}$, $T_{end}$, and subsequently the duration of the event $T_{dur}$. See detailed description in the Methods section. Insert: An arrow highlights the analysed endocytotic event (5x5 pixels area). (C) Averaged profile from individual Myo1 (blue) and Cam1 (red) membrane association events, synchronised relative to $T_{start}$ and $T_{end}$. Dotted lines show fitted rising (Myo1: 537 AU/sec, Cam1: 1073 AU/sec) and falling (Myo1: 567 AU/sec, Cam1: 1028 AU/sec) gradients. (D) An example fluorescence trace from simultaneously two-colour imaging Myo1 (blue line) and Cam1 (red line) membrane association event observed in *mNeongreen.myo1 cam1.mCherry* cells is consistent with relative intensities and timings observed using single fluorophore strains. (E) Averaged intensity trajectories of individual Myo1 (blue line) and Myo1.S742A (red line) endocytosis events from TIRFM imaging of *mNeongreen.myo1* and *mNeongreen.myo1.S742A* cells respectively.

**Figure 4. Myo1 S742 is phosphorylated in a cell cycle dependent manner**

**to affect polarised growth.** (A) Western blots of extracts from $G_1$ arrested *cdc10.v50* cells, and pre-mitotic $G_2$ arrested *cdc25.22* cells probed with phospho-specific anti-Myo1$^{S742}$ (upper panel) and anti-Myo1 (lower panel) antibodies demonstrate Myo1 $^{S742}$ phosphorylation occurs prior to the Cdc10 execution point in monopolar G1 cells, and is not detectable by the Cdc25 execution point at end of G2 (n=3). (B - D) A *cdc10.v50* culture was synchronized in G1 by shifting to 36 °C for 240 min before returning to 25 °C at time 0. Samples of cells were taken every 20 min from the release and processed for western blotting to monitor Myo1$^{S742}$ phosphorylation. The membrane was first probed with phosphospecific anti-Myo1$^{S742}$* antibodies (B) and subsequently probed with anti-Myo1 antibodies (C) to monitor total Myo1. Both phosphorylated (1) and non-phosphorylated (2) Myo1 bands can be observed in B. Equal loading was monitored by Ponceau staining of the membrane. (D) Densitometry measurements of phosphorylated Myo1$^{S742}$ (from B) and total Myo1 (both bands from C) are plotted along with the % of cells in the culture with septa. (E) Myosin-1 distribution (green), calcofluor stained regions of cell growth (magenta) and cell outline (transmitted image) of prototroph *mNeongreen.myo1*$^{+}$ and *mNeongreen.myo1.S742A* cells cultured in EMMG at 34 ºC. Asterisks highlight cells with morphology defects. Scale: 10 µm. (F) Calcofluor stained WT and *myo1.S742A* cells. Asterisks highlight long bent cells displaying monopolar growth. Scale - 5 µm.

**Figure 5. Myo1$^{S742}$ phosphorylation impacts polarised cell growth.** (A) Average length and frequency of growth defects in wt, *myo1.S742A*, *tea4*Δ, *cam2*Δ, *tea4*Δ *myo1.S742A*, and *tea4*Δ *cam2*Δ cells. (B) Ratio of Sla2-mCherry fluorescence at “new”: “old” cell end, averaged from >30 growing mid-log *sla2-mCherry myo1*$^{+}$ (upper panel) and *sla2-mCherry myo1.S742A* (lower panel) cells. Boxes plot median and quartile for each length measured, lines are plotted from the mean average value at each length measured. (C) Averaged growth curves from 3 independent experiments of prototroph wild type (empty circles) and *myo1.S742A* (grey filled circles) cells cultured in EMMG at 34 ºC. Slower growth is apparent at the end of log phase in

*myo1.S742A* cells, which go grow more until reaching stationary phase. Error bars denote s.d.

**Figure 6. Cam2 associates with internalised endocytic vesicles.** (A) Kymographs of GFP labelled foci from maximum projections of 13-z plane timelapse images of *mNeongreen.myo1* (upper panel), *cam1.gfp* (middle panel) and *cam2.gfp* (bottom panel) cells illustrate the static nature of Myo1 and Cam1 endocytic foci when associated with the plasma membrane (black arrows). Spindle Pole Body (asterisk) associated Cam1 foci are highlighted. In contrast Cam2 foci displayed extensive lateral movements. (B) Kymographs generated from single z-plane timelapse images of single endocytic foci surface during vesicle formation and subsequent internalisation. While Myo1 and Cam1 only associate with the plasma membrane, Cam2, Sla2 and actin are internalised on the vesicle after scission. These kymographs are not aligned temporally. (C) Kymographs of Cam2 and Sla2 co-internalisation in *sla2.mCherry cam2.gfp* cells. (D) Maximum projection of 31-z slice image of *cam1.mCherry cam2.gfp* cells reveals Cam1 (magenta) and Cam2 (green) colocalise in a subset of endocytic foci. (E-G) Single frames (left panels) and kymographs (right panels) from maximum projections of 13-z plane timelapse images of *cam1.gfp* (E), *cam2.gfp* (F) and *LifeACT.mCherry* (G) in either *myo1*$^{+}$ (upper panels) or *myo1*$\Delta$ (lower panels) cells. These show while only Cam1 recruitment to endocytic foci is dependent upon Myo1, the myosin is required for internalisation of Cam2-GFP and LifeACT.mCherry foci. Scales: 5 µm.

**Figure 7. Cam2 does not impact Myo1 or Cam1 dynamics in vegetative cells.** (A) An example fluorescence trace of a Cam2 membrane binding and vesicle internalisation event from TIRFM imaging of *cam2.gfp* cells. An abrupt drop in the fluorescence was marked as "scission time" ($T_{scis}$, grey vertical line). Insert: An arrow shows the location of the monitored endocytic event (5x5 pixels area). (B) Averaged profile from 65 individual Cam2 membrane association events (green line), together with averaged Cam1-mCherry profile (red) from two-colour TIRFM imaging of *cam1.mCherry cam2.gfp* cells.

Events were synchronized relative to Cam1 $T_{start}$. Grey line denotes mean time of vesicle scission ($T_{scis}$). See detailed description in the Methods section. (C) Maximum projection of 31-z slice widefield image of a mixture of *yfp.myo1 sid4.tdTomato* (wt - with a red labelled spindle pole body marker) and *yfp.myo1 cam2*Δ (asterisks) cells. Red labelled SPBs allows differentiation between *cam2*$^{+}$ and *cam2*Δ cells in the same field. (D) Maximum projection of 31-z slice widefield image of a mixture of prototroph *cam1.gfp sid4.tdTomato* (wt – with a red labelled spindle pole body marker) and *cam1.gfp cam2*Δ (asterisks) cells. Red labelled SPBs allows differentiation between *cam2*$^{+}$ and *cam2*Δ cells in the same field. Scales – 5 µm.

**Figure 8. Myo1 S742 phosphorylation regulated Cam1 and Cam2 dynamics during meiosis.** (A) Kymographs of Cam2.GFP foci dynamics in *myo1*$^{+}$ (upper panel) and *myo1.S742A* (lower panel) cells. (B) Scheme of consequence of phosphorylation of Myo1$^{Ser742}$ (small empty circle) and $Ca^{2+}$ levels upon Cam1 (light grey filled circle) and Cam2 (dark grey filled circle) binding to the IQ1 (solid thick black line) and IQ2 (compound line) motifs of Myo1, and impact on relative orientation of the myosin lever arm (dashed arrow). Highlighted combination of unphosphorylated Myo1$^{S742}$ & $Ca^{2+}$ does not normally occur in cells. (C) Western blots of extracts from G1 arrested *cdc10.v50 myo1*$^{+}$, *cdc10.v50 myo1-S742A*, and conjugation arrested (starved, premeiotic cells) *fus1*Δ cells, as well as meiotic spores, probed with phospho-specific anti-Myo1$^{S742}$ antibodies (upper panel; ponceau staining lower panel) confirm Myo1S742 remains phosphorylated from the end of G1, through conjugation until the end of meiosis (n=5). Relative Myo1$^{S742}$ phosphorylation levels were calculated from 3 independent equivalent experiments (mean ± sd). (D) Maximum projection of 13-z slice GFP fluorescence image and transmitted light image from a timelapse of vegetative (cell 1) and meiotic (cell 2) *gfp-act1* cells. Image from a GFP-act signal. Kymographs in the right panels were generated along the two dotted axes. (E) Maximum projection of mNeongreen-Myo1 fluorescence (left), FM4-64 fluouresence (middle) and transmitted light images of a mixed population of vegetative, fusing (*) and sporulating (**) *mNG-myo1*$^{+}$ cells, illustrate endocytosis is reduced in meiotic

cells. Scale - 10 µm. (F) Micrographs of *myo1.S742A* cell morphology on solid starvation media. Asterisks - cells with unregulated growth and polarity defects; arrows - cells with elongated or abnormally bent shmooing (conjugation) tips; arrow heads - meiotic cells with defective spore formation. Scale – 5 µm. (G) A schematic of the TORC2 - Gad8 - Myo1$^{S742}$ signalling pathway.

## Supplementary Data Legends

**Figure 2-figure supplement 1. Purified proteins used during *in vitro* studies.** Coomassie stained SDS-PAGE gel of recombinant proteins expressed and purified during this study. From left to right lanes contain (L) protein standard; (1) Nt-acetylated Cam1; (2) Nt-acetylated Cam1-T6C; (3) Cam1-FRET; (4) Cam2; (5) IQ12 peptide (not used during this study); (6) Myo1IQ12-FRET; and (7) Myo1IQ12S742D-FRET.

**Figure 2-figure supplement 2. Cam1 and Cam2 do not interact directly.** (A) Overlaid $OD_{280}$ spectra were recorded of eluate from a Superdex 75 gel filtration column which had been loaded with either Cam1 (grey line), Cam2 (black line) or both Cam1 and Cam2 (red line) under identical 4 mM EGTA buffer conditions. (B) Maximum IAANS fluorescence values (440 nm) of 0.5 μM Cam1-IAANS at a range of pCa values. Black symbols show values of Cam1-IAANS, red symbols show values of Cam1-IAANS with 5 μM Cam2 protein. 2 mM Ca- EGTA buffers were used to give indicated pCa values. $pCa_{50}$ values calculated from Origin fitting analysis - Hill equation.

**Figure 3-figure supplement 1. Relative TIRF profiles.** (A) Maximum projections of 31-z stack widefield images of *mNG.myo1, cam1.gfp* and *cam2.gfp* cells (Scales - 5 μm). (B) Combined profiles of averaged intensity trajectories of Myo1 (blue) and Cam1 (red) endocytosis events in wild type (solid lines) or *myo1.S742A* strains (dashed lines). TIRF imaging, see Methods section for the description. Insert: The distribution of the durations of individual wild type Myo1 events.

**Supplementary File 1**: *Strains used during this study.*

**Supplementary File 2**: *Oligonucleotides used during this study.*

**Video 1**: Single molecule Myo1 membrane association events. TIRFM imaging of *mNeongreen.myo1* cell showing rapid single molecule interactions of Myo1 with the plasma membrane, apparent as small bright green spots of a diffraction limited size, visible over background from the camera noise (highlighted by tracking white lines). These single myosin1 molecules have

limited residency time (off rate 7.8 $s^{-1}$) and mobility (0.03 $\mu m^2.s^{-1}$) at the plasma membrane. 63 fps @ 23°C. The plot at the end of the Video was constructed from analysis of a 50 sec full length Video.

**Video 2**: Endocytic Myo1 events. TIRFM imaging of *mNeongreen.myo1* cells showing endocytosis associated interactions of Myo1 at the plasma membrane. The myosin1 quickly accumulates at the site of endocytosis and 5-8 seconds of reaching a maximum, rapidly leaves the endocytic site. The accumulated myosin remains immobile on the membrane for the duration of the event. 20 fps @ 23°C.

**Video 3**: Endocytic Cam1 events. TIRFM imaging of *cam2.gfp* cell showing Cam2 recruiting to endocytic vesicles, to which it remains associated after scission and internalisation of the endosome. At the start of each event each spot is immobile, but at the end of endocytic event the vesicle oscillates as it is internalised into the cytoplasm. 20 fps @ 23°C.

**Video 4**: Comparison of Cam1 and Cam2 dynamics. TIRFM imaging of *cam1.mCherry cam2.gfp* cell showing early recruitment of Cam1 (red) and subsequent recruitment of Cam2 (green) to the sites of endocytosis. Cam1 disassociates prior to vesicle scission, while Cam2 remains associated with the internalised endosome, so that at the beginning of the endocytic event the spots are red, but during the event they became yellow as Cam2 (green) is recruited to the vesicle. At the end of the event vesicle became green as Cam1 dissociates from the endocytotic site. 20 fps @ 23°C.

**Video 5**: Myo1 dynamics in interphase and meiotic cells. Timelapse of maximum projections from 13-z slice widefield images of *mNeongreen.myo1* cells showing typical examples of Myo1 dynamics in vegetative and meiotic (highlighted with arrow) cells. Frame rate: 650 msec / frame.

**Video 6**: Cam1 dynamics in interphase and meiotic cells. Timelapse of maximum projections from 13-z slice widefield images of *cam1.gfp* cells showing typical examples of Cam1 dynamics in vegetative and meiotic (highlighted with arrow) cells. Frame rate: 650 msec / frame.

**Video 7**: Cam2 dynamics in interphase and meiotic cells. Timelapse of maximum projections from 13-z slice widefield images of *cam2.gfp* cells showing typical examples of Cam2 dynamics in vegetative and meiotic (highlighted with arrow) cells. Frame rate: 650 msec / frame.

**Video 8**: Act1 dynamics in interphase and meiotic cells. Timelapse of maximum projections from 13-z slice widefield images of *gfp.act1* cells showing typical examples of Act1 dynamics in vegetative and meiotic (highlighted with arrow) cells. Frame rate: 650 msec / frame.

**Supplementary File 1**: Strains used during this study.

**Supplementary File 2**: Oligonucleotides used during this study.

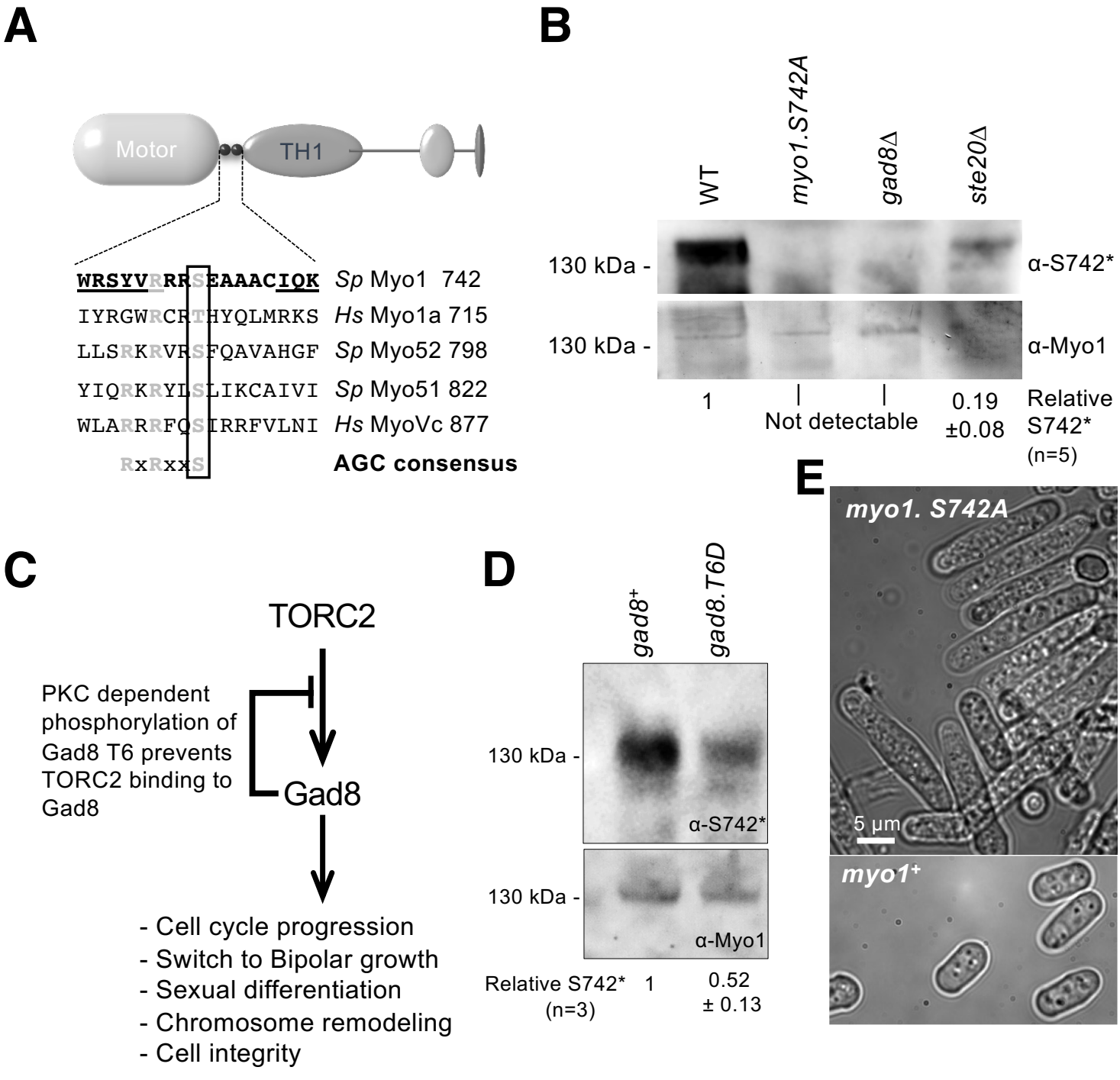
A
Motor
TH1
WRSYVRRRSEAAACIQK Sp Myo1 742
IYRGWRCRTHYQLMRKS Hs Myo1a 715
LLSRKRVRSFQAVAHGF Sp Myo52 798
YIQRKRYLSLIKCAIVI Sp Myo51 822
WLARRRFQSIRRFVLNI Hs MyoVc 877
RxRxxS AGC consensus
B
WT
myo1.S742A
gad8Δ
ste20Δ
130 kDa -
α-S742*
130 kDa -
α-Myo1
1
Not detectable
0.19 ±0.08
Relative S742* (n=5)
C
TORC2
PKC dependent phosphorylation of Gad8 T6 prevents TORC2 binding to Gad8
Gad8
- Cell cycle progression
- Switch to Bipolar growth
- Sexual differentiation
- Chromosome remodeling
- Cell integrity
D
gad8+
gad8.T6D
130 kDa -
α-S742*
130 kDa -
α-Myo1
Relative S742* (n=3)
1
0.52 ± 0.13
E
myo1. S742A
5 μm
myo1+

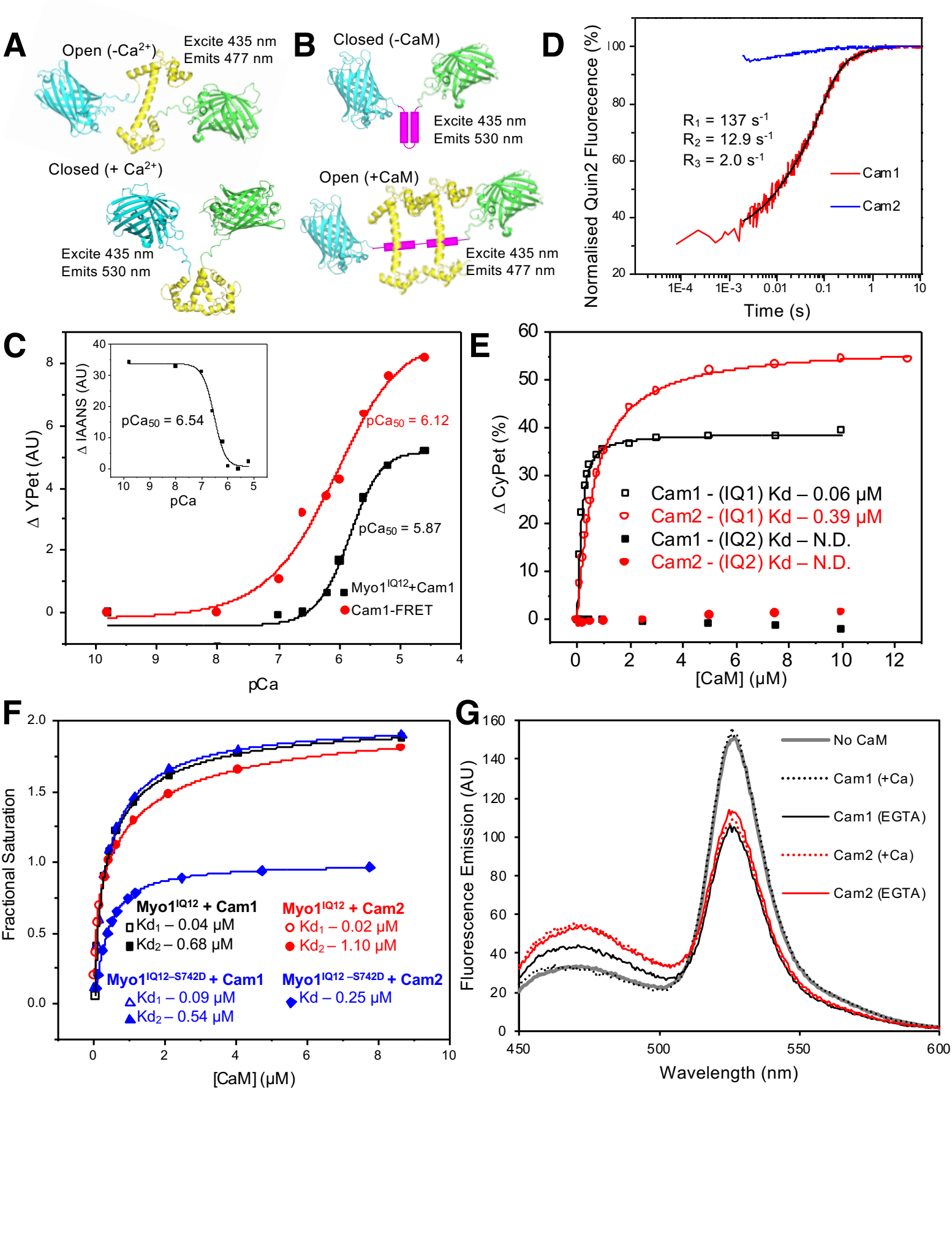
A
Open (-Ca2+)
Excite 435 nm
Emits 477 nm
Closed (+ Ca2+)
Excite 435 nm
Emits 530 nm
B
Closed (-CaM)
Excite 435 nm
Emits 530 nm
Open (+CaM)
Excite 435 nm
Emits 477 nm
D
Normalised Quin2 Fluorecence (%)
R1 = 137 s-1
R2 = 12.9 s-1
R3 = 2.0 s-1
Cam1
Cam2
Time (s)
C
Δ YPet (AU)
Δ IAANS (AU)
pCa50 = 6.54
pCa
pCa50 = 6.12
pCa50 = 5.87
Myo1IQ12+Cam1
Cam1-FRET
pCa
E
Δ CyPet (%)
Cam1 - (IQ1) Kd – 0.06 μM
Cam2 - (IQ1) Kd – 0.39 μM
Cam1 - (IQ2) Kd – N.D.
Cam2 - (IQ2) Kd – N.D.
[CaM] (μM)
F
Fractional Saturation
Myo1IQ12 + Cam1
Kd1 – 0.04 μM
Kd2 – 0.68 μM
Myo1IQ12 + Cam2
Kd1 – 0.02 μM
Kd2 – 1.10 μM
Myo1IQ12–S742D + Cam1
Kd1 – 0.09 μM
Kd2 – 0.54 μM
Myo1IQ12 –S742D + Cam2
Kd – 0.25 μM
[CaM] (μM)
G
Fluorescence Emission (AU)
No CaM
Cam1 (+Ca)
Cam1 (EGTA)
Cam2 (+Ca)
Cam2 (EGTA)
Wavelength (nm)

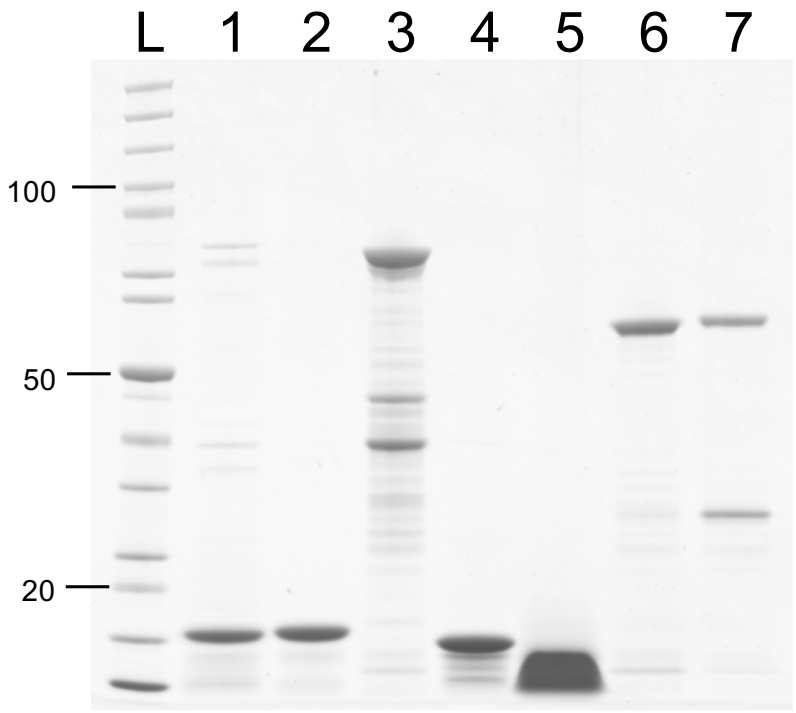


L – Ladder
1 – Cam1-ACE
2 – Cam1-IAANS
3 – Cam1-FRET
4 – Cam2
5 – IQ12 peptide – not used in study
6 – Myo1IQ12 FRET
7 – Myo1IQ12-S742D FRET

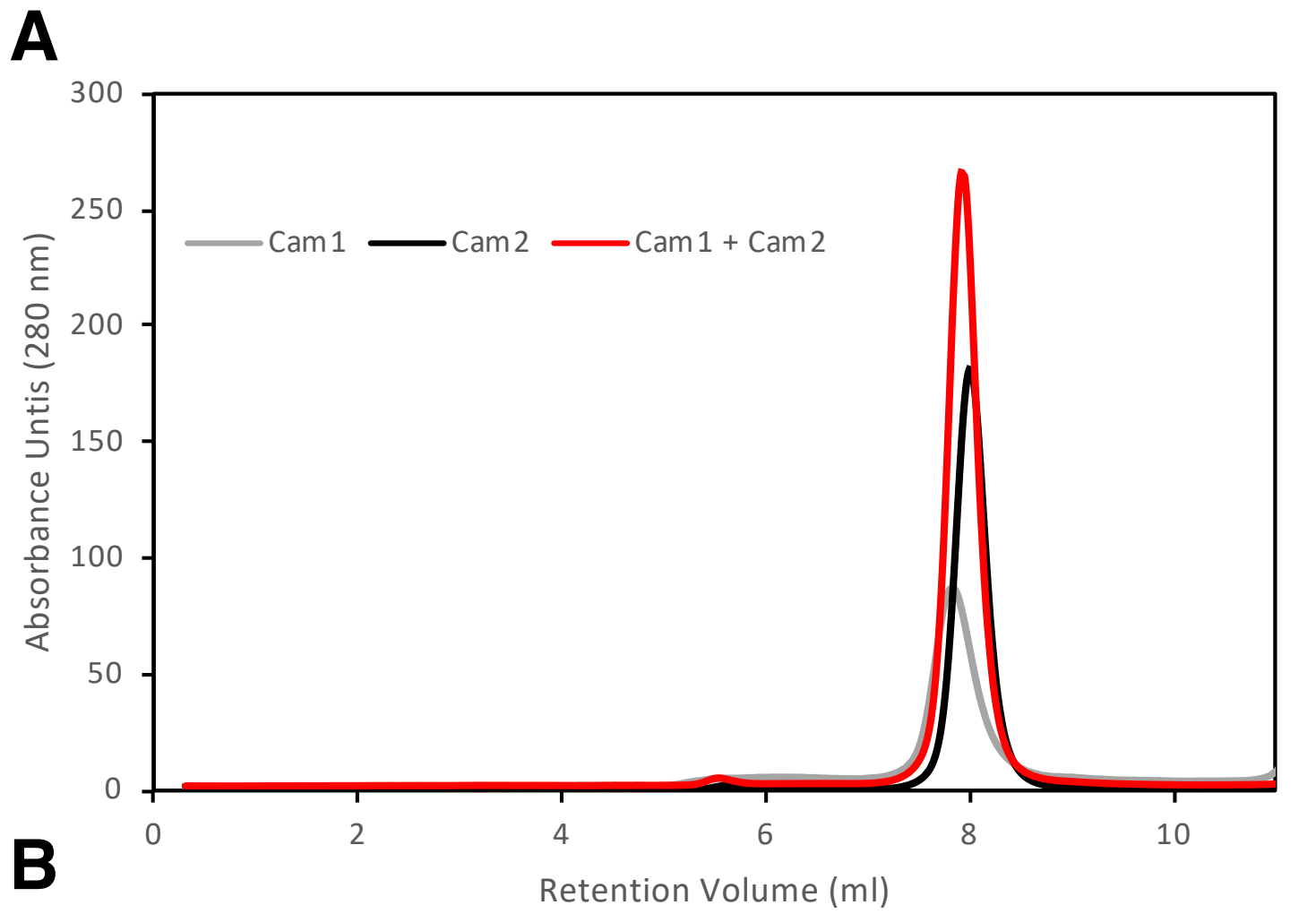
A
Absorbance Untis (280 nm)
Retention Volume (ml)
Cam 1
Cam 2
Cam 1 + Cam 2
0
50
100
150
200
250
300
0
2
4
6
8
10

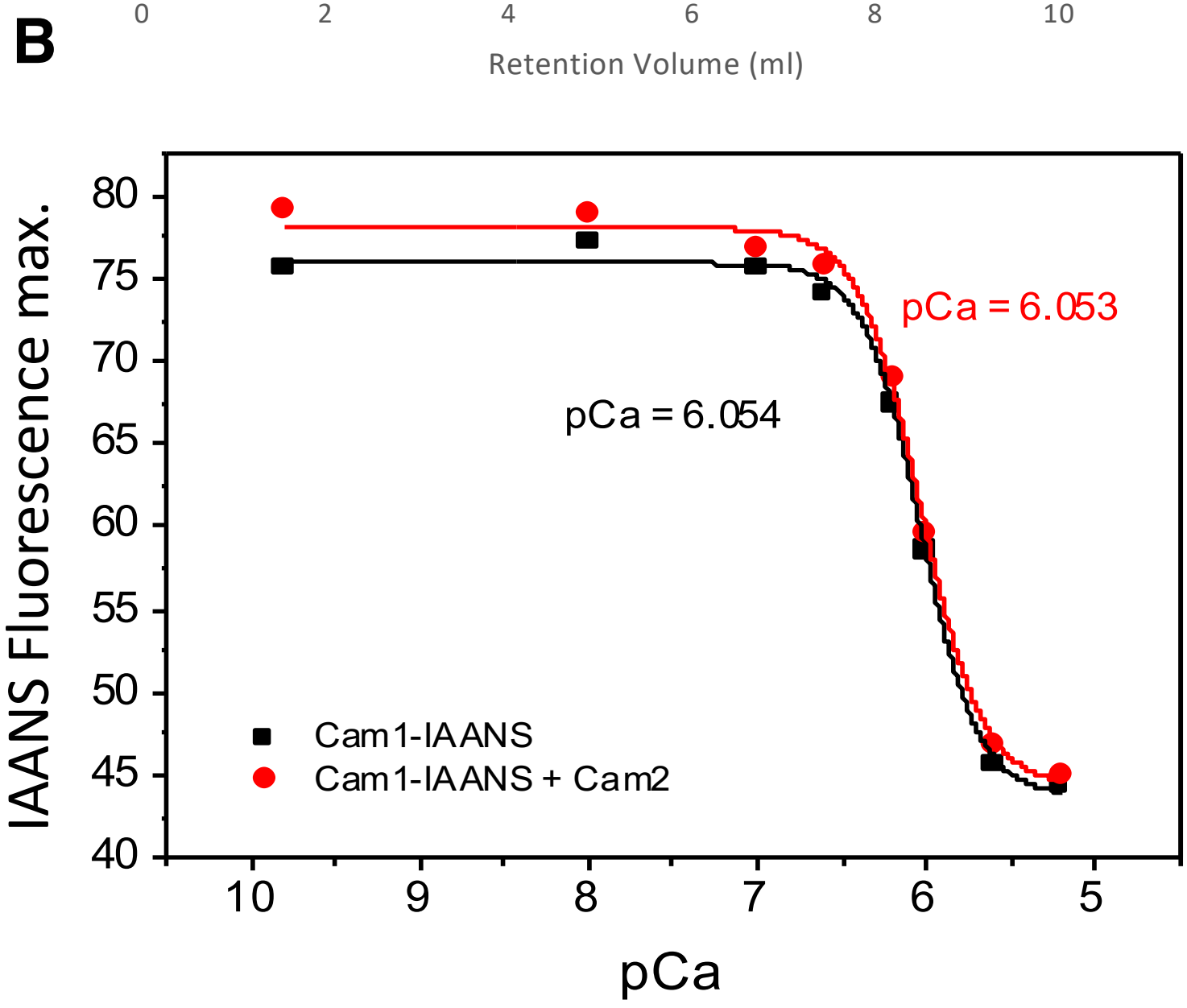
B
IAANS Fluorescence max.
pCa
pCa = 6.053
pCa = 6.054
Cam1-IAANS
Cam1-IAANS + Cam2
40
45
50
55
60
65
70
75
80
10
9
8
7
6
5

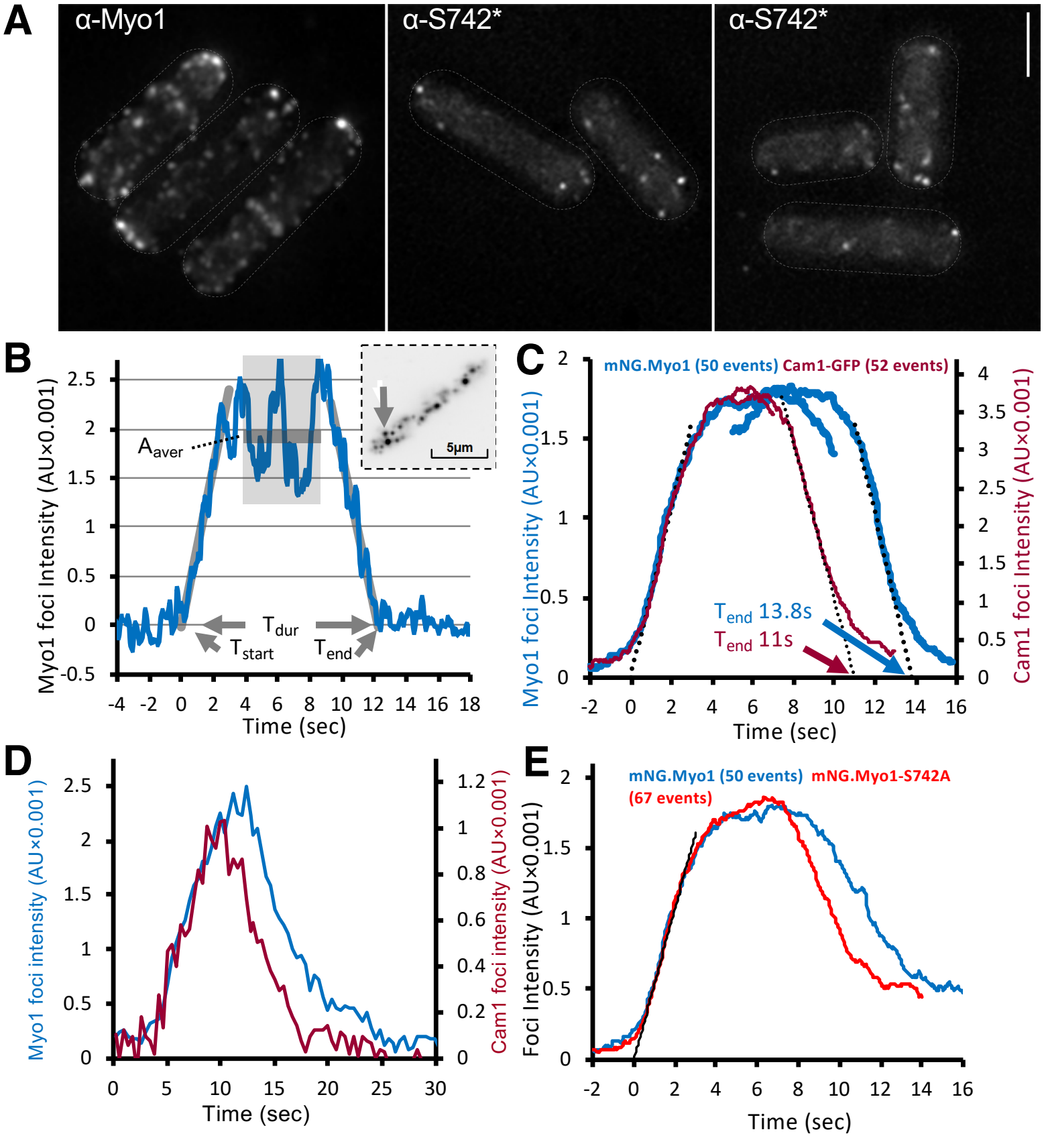
A
α-Myo1
α-S742*
α-S742*
B
Myo1 foci Intensity (AU×0.001)
Aaver
Tdur
Tstart
Tend
5μm
Time (sec)
C
mNG.Myo1 (50 events) Cam1-GFP (52 events)
Myo1 foci Intensity (AU×0.001)
Cam1 foci Intensity (AU×0.001)
Tend 13.8s
Tend 11s
Time (sec)
D
Myo1 foci intensity (AU×0.001)
Cam1 foci intensity (AU×0.001)
Time (sec)
E
mNG.Myo1 (50 events) mNG.Myo1-S742A (67 events)
Foci Intensity (AU×0.001)
Time (sec)

A

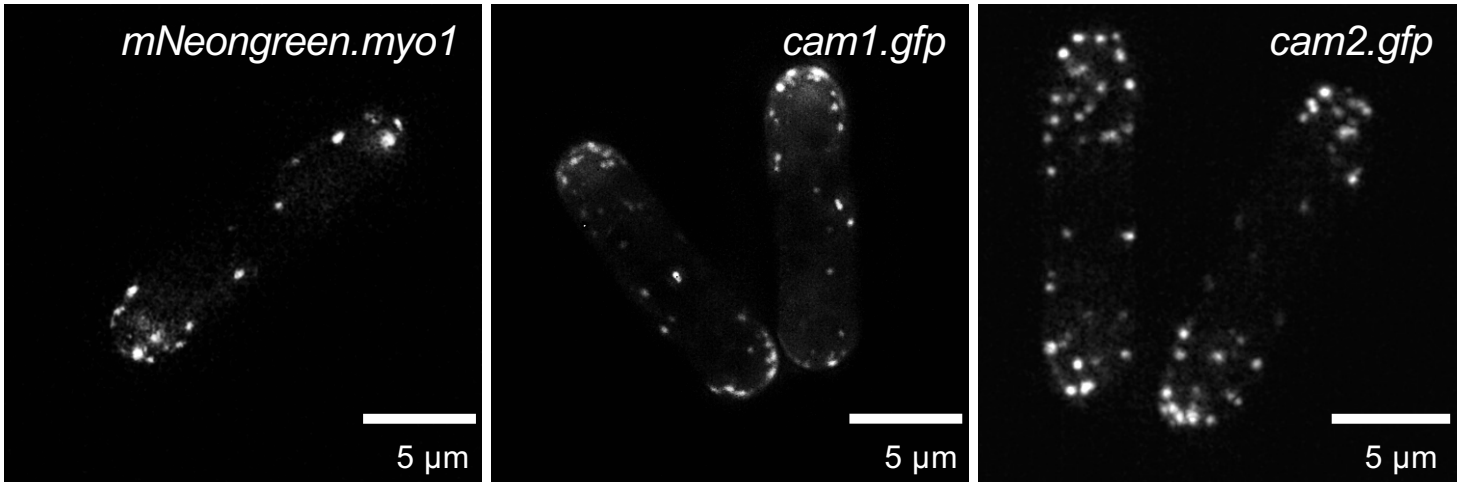
mNeongreen.myo1
5 µm
cam1.gfp
5 µm
cam2.gfp
5 µm

B

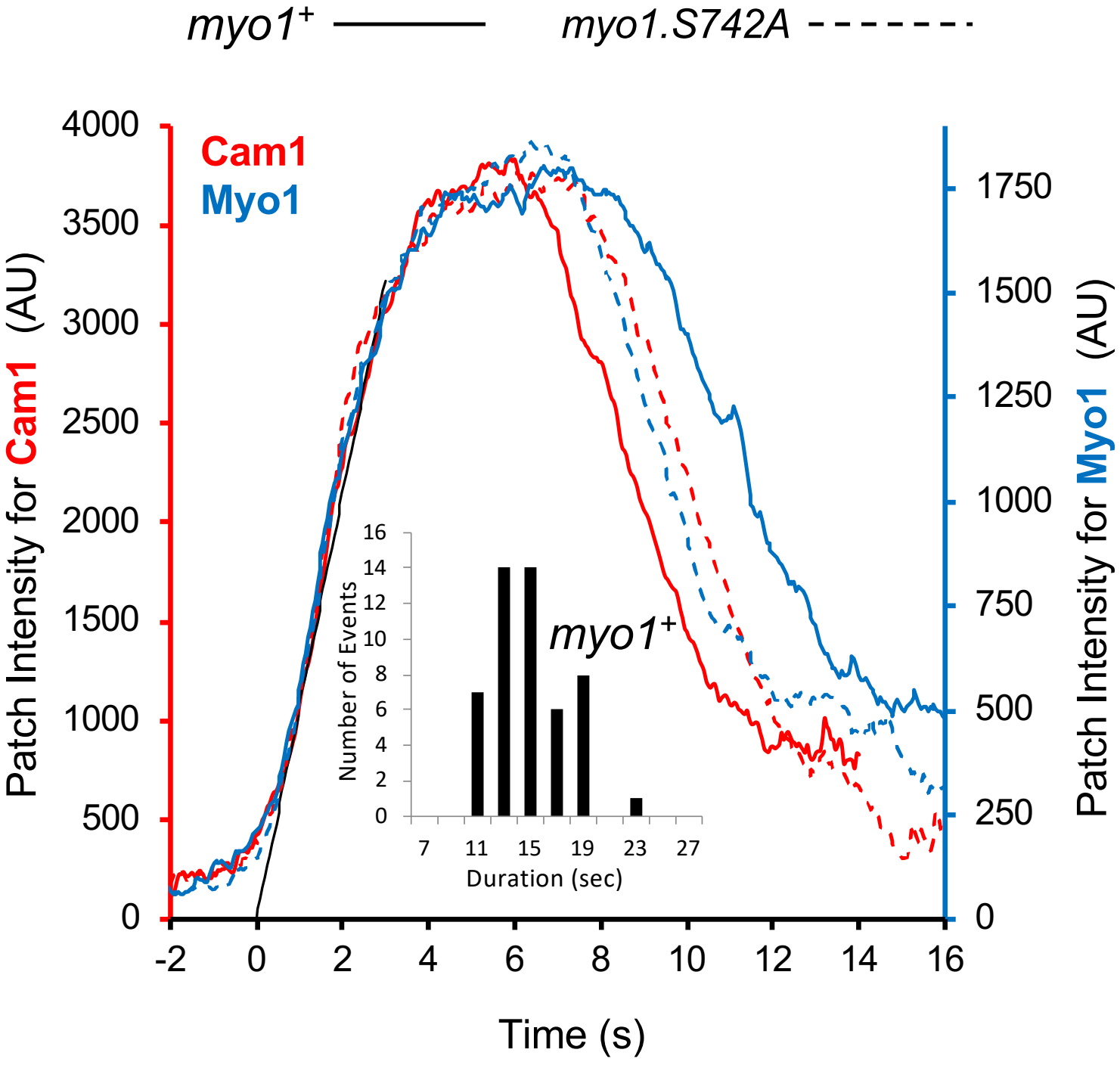
myo1+
myo1.S742A
Cam1
Myo1
Patch Intensity for Cam1 (AU)
Patch Intensity for Myo1 (AU)
Time (s)
Number of Events
Duration (sec)
myo1+

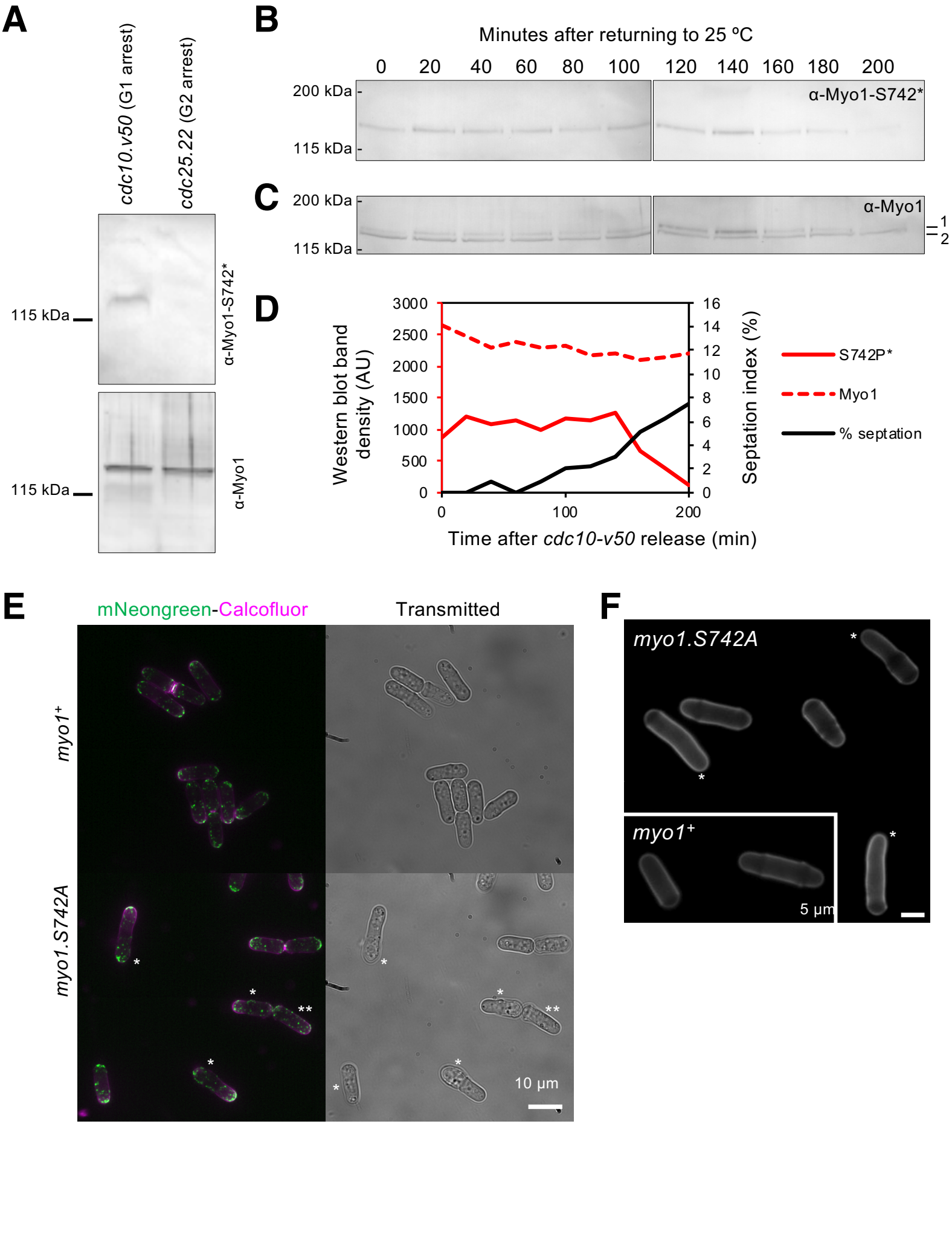
A
cdc10.v50 (G1 arrest)
cdc25.22 (G2 arrest)
115 kDa
α-Myo1-S742*
115 kDa
α-Myo1
B
Minutes after returning to 25 ºC
0 20 40 60 80 100 120 140 160 180 200
200 kDa
115 kDa
α-Myo1-S742*
C
200 kDa
115 kDa
α-Myo1
1
2
D
Western blot band density (AU)
Septation index (%)
Time after cdc10-v50 release (min)
S742P*
Myo1
% septation
E
mNeongreen-Calcofluor
Transmitted
myo1+
myo1.S742A
10 µm
F
myo1.S742A
myo1+
5 µm

**A**

| | wt | *myo1.S742A* | *tea4Δ* | *cam2Δ* | *tea4Δ myo1.S742A* | *tea4Δ cam2Δ* |
|---|---|---|---|---|---|---|
| Average cell length (μm) | 9.77 | 13.2 | 12.5 | 13.2 | 12.5 | 12.7 |
| % Bent >5º off long axis | 0.4 | 24.7 | 51.7 | 18.3 | 49.4 | 66.7 |
| % multiple growth zones | 0.0 | 0.0 | 5.7 | 0.0 | 4.6 | 18.9 |
| n | >500 | >500 | 88 | 83 | 88 | 91 |

**B**

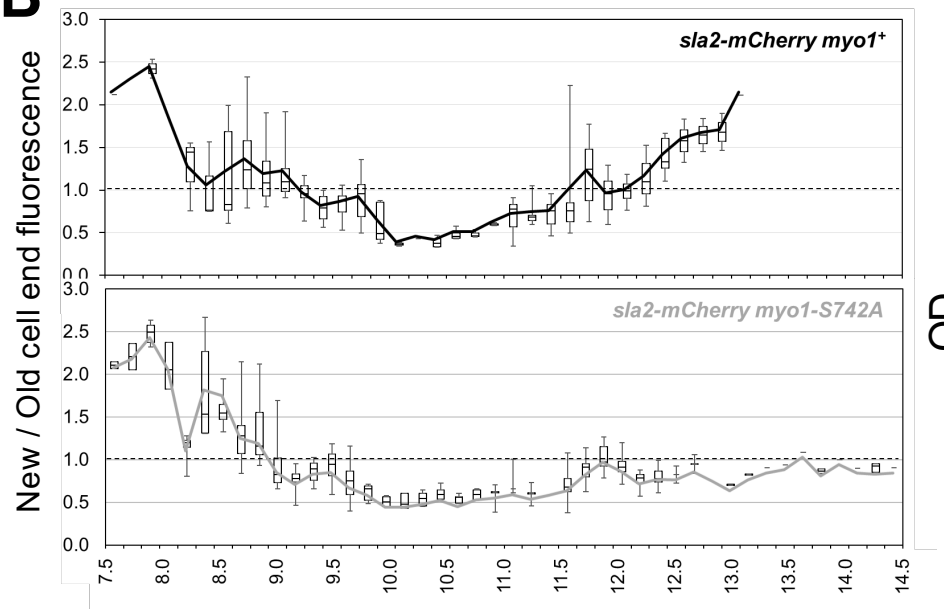


**C**

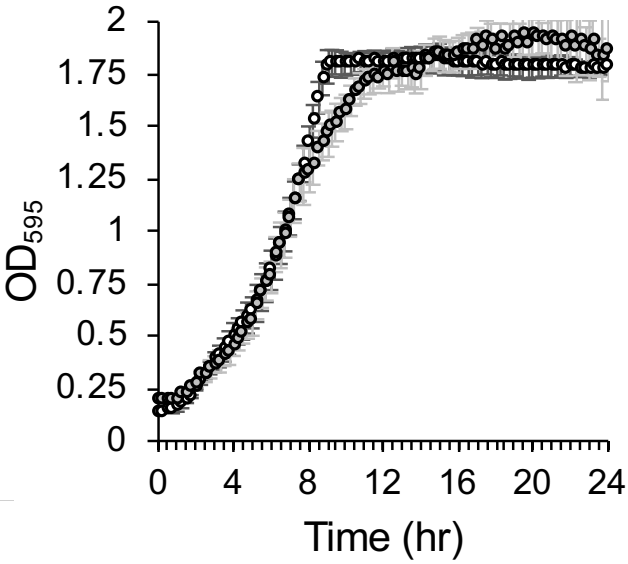

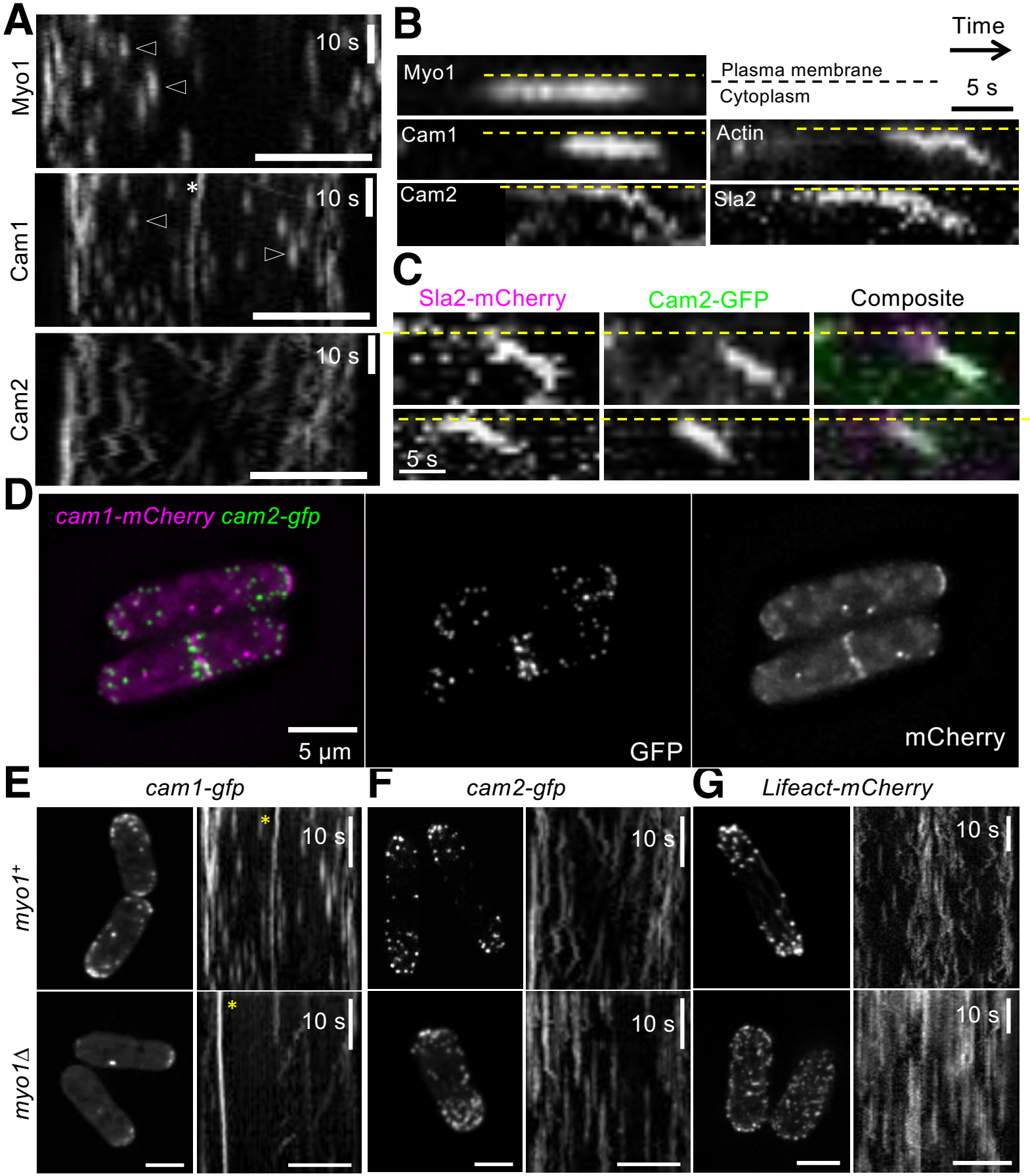
A
Myo1
10 s
Cam1
10 s
Cam2
10 s
B
Time
Myo1
Plasma membrane
Cytoplasm
5 s
Cam1
Actin
Cam2
Sla2
C
Sla2-mCherry
Cam2-GFP
Composite
5 s
D
cam1-mCherry cam2-gfp
5 μm
GFP
mCherry
E
cam1-gfp
myo1+
10 s
myo1Δ
10 s
F
cam2-gfp
10 s
10 s
G
Lifeact-mCherry
10 s
10 s

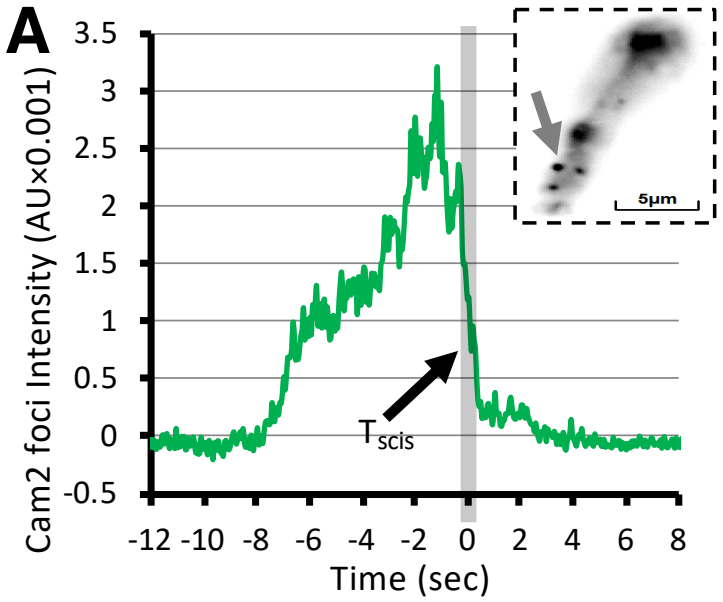


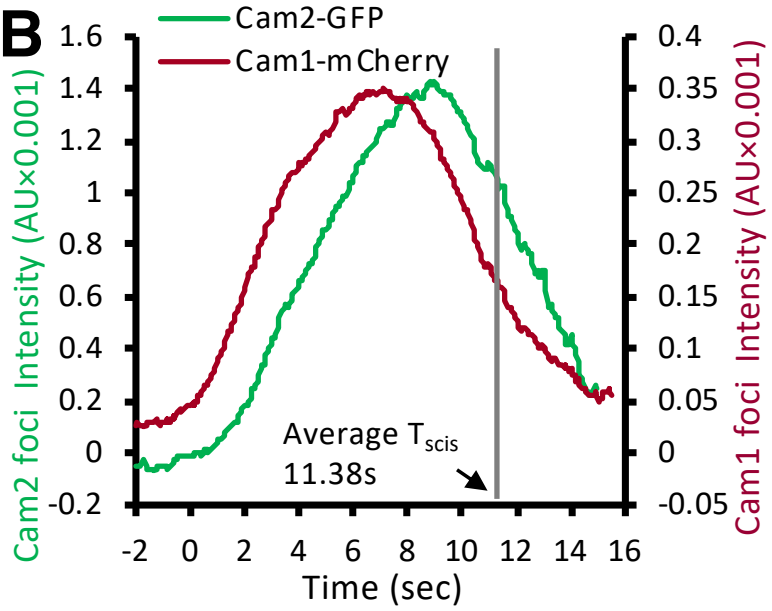


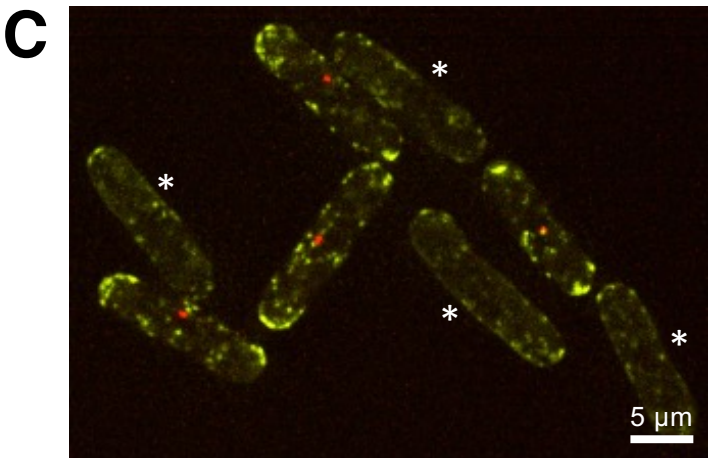


*yfp.myo1⁺ sid4.tdTomato* (SPB) *cam2⁺* and *myo1⁺ cam2Δ* (*) cells

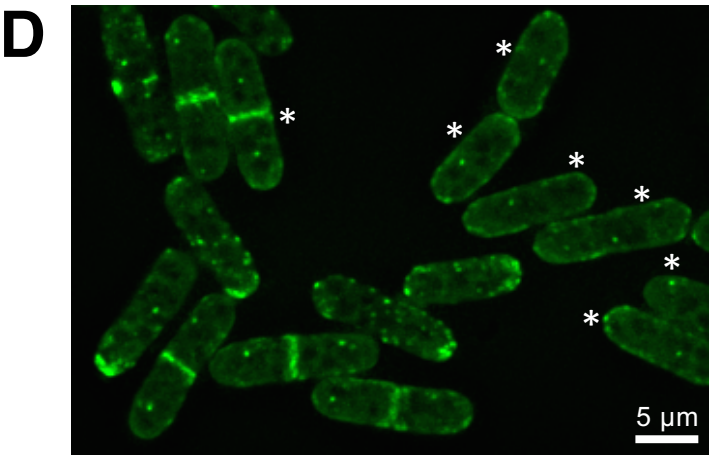


*cam1.gfp sid4.tdTomato* (SPB) *cam2⁺* and *cam1.gfp cam2Δ* (*) cells

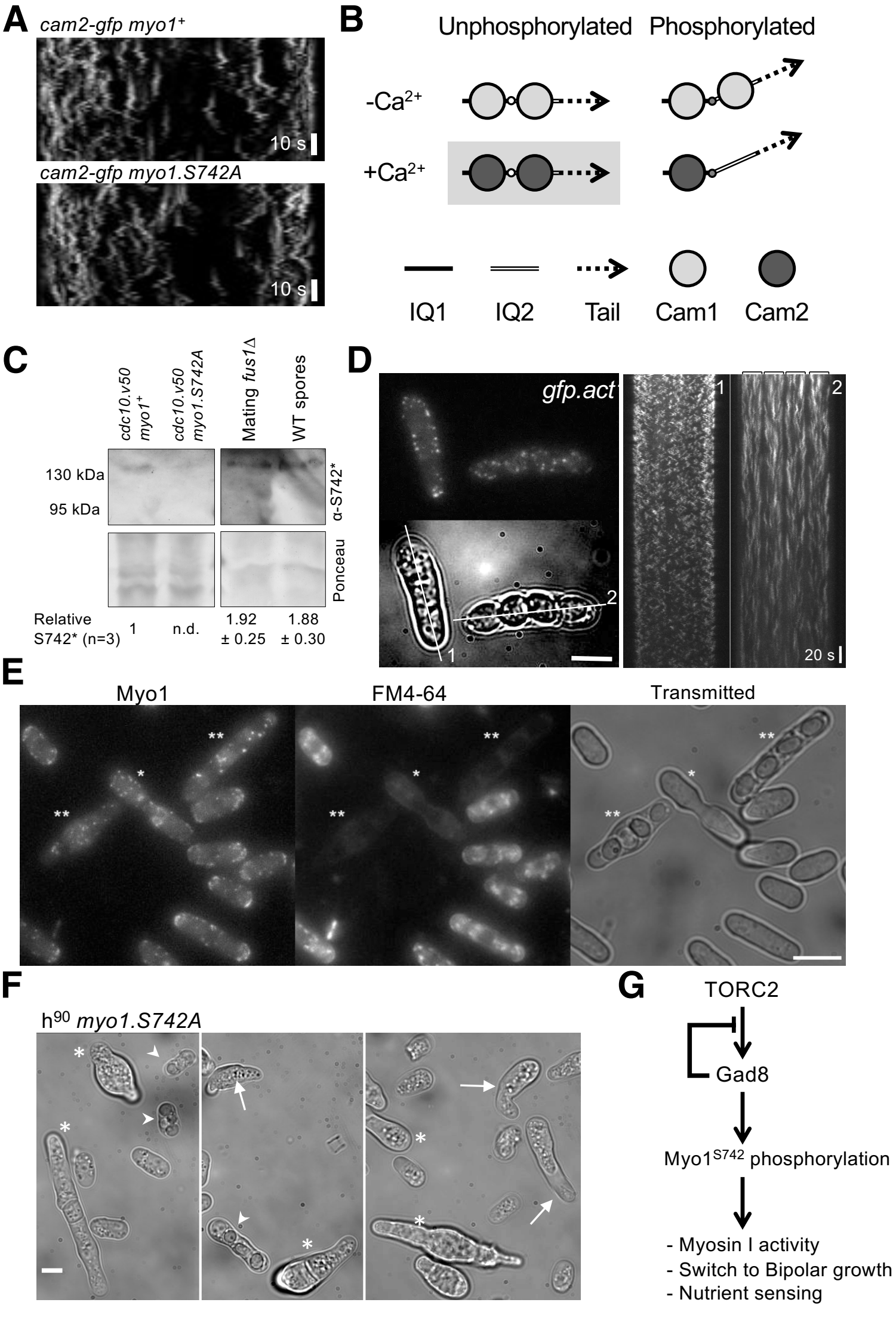
A
cam2-gfp myo1+
10 s
cam2-gfp myo1.S742A
10 s
B
Unphosphorylated
Phosphorylated
-Ca2+
+Ca2+
IQ1
IQ2
Tail
Cam1
Cam2
C
cdc10.v50 myo1+
cdc10.v50 myo1.S742A
Mating fus1Δ
WT spores
130 kDa
95 kDa
α-S742*
Ponceau
Relative S742* (n=3)
1
n.d.
1.92 ± 0.25
1.88 ± 0.30
D
gfp.act
1
2
20 s
E
Myo1
FM4-64
Transmitted
F
h90 myo1.S742A
G
TORC2
Gad8
Myo1S742 phosphorylation
- Myosin I activity
- Switch to Bipolar growth
- Nutrient sensing